




Water Resources Research



RESEARCH ARTICLE

10.1029/2023WR035595

Pore-Scale Modeling of Water and Ion Diffusion in Partially Saturated Clays

Yuankai Yang¹ , Sergey V. Churakov^{2,3}, Ravi A. Patel⁴, Nikolaos Prasianakis³, Guido Deissmann¹ , Dirk Bosbach¹ , and Jenna Poonoosamy¹

¹Institute of Energy and Climate Research—Nuclear Waste Management (IEK-6), JARA-CSD, Forschungszentrum Jülich GmbH, Jülich, Germany, ²Laboratory for Waste Management, Paul Scherrer Institut, Villigen, Switzerland, ³Institute of Geological Sciences, University of Bern, Bern, Switzerland, ⁴Institute of Building Materials and Concrete Structures (IMB), Karlsruhe Institute of Technology (KIT), Karlsruhe, Germany

Key Points:

- Development of a pore-scale numerical framework to simulate water and ion diffusion in partially saturated clays
- Derivation of an equivalent solute method to improve the numerical stability caused by the discontinuities at the water/vapor interface
- The electrical double layer has a stronger effect on ion transport under unsaturated conditions than under water saturated conditions

Correspondence to:

Y. Yang,
y.yang@fz-juelich.de

Citation:

Yang, Y., Churakov, S. V., Patel, R. A., Prasianakis, N., Deissmann, G., Bosbach, D., & Poonoosamy, J. (2024). Pore-scale modeling of water and ion diffusion in partially saturated clays. *Water Resources Research*, 60, e2023WR035595. <https://doi.org/10.1029/2023WR035595>

Received 19 JUN 2023
Accepted 22 DEC 2023

Author Contributions:

Conceptualization: Yuankai Yang
Investigation: Yuankai Yang, Ravi A. Patel
Methodology: Yuankai Yang, Sergey V. Churakov, Ravi A. Patel
Project Administration: Dirk Bosbach
Supervision: Nikolaos Prasianakis, Guido Deissmann, Dirk Bosbach, Jenna Poonoosamy
Writing – original draft: Yuankai Yang, Jenna Poonoosamy
Writing – review & editing: Sergey V. Churakov, Ravi A. Patel, Nikolaos Prasianakis, Guido Deissmann, Dirk Bosbach

Abstract An accurate mechanistic understanding of solute diffusion in partially saturated clays is critical for assessing the safety of deep geological repositories for radioactive waste. In this study, a pore-scale numerical framework is developed to simulate water and ion diffusion in partially saturated clays. First, the two-phase Shan-Chen Lattice Boltzmann method is employed to establish the liquid-gas distribution in a reconstructed three-dimensional pore geometry of a clay. An equivalent solute method is also developed and validated to improve the numerical stability of the solution at the liquid/gas interface corresponding to steep variations of the concentration and diffusion coefficient of the water tracer. By using a mobility-distance relationship from molecular simulations, Fick's law is numerically solved to simulate water diffusion in nanopores, while the coupled Poisson-Boltzmann-Nernst-Planck equations are solved to simulate ion diffusion under the influence of the electrical double layer (EDL). Our model reveals that the decrease of relative effective diffusion coefficients during the desaturation is more pronounced for ions than for water, due to the additional transport pathway of water tracers in the gas phase. The obtained effective diffusion coefficients of tritiated water and ions agree well with reported data from compacted sedimentary rocks. By comparing the local electric potential and the distribution of ion concentrations in single pores, the simulation results suggest that the EDL in unsaturated clays has a more complex influence on ion distribution than under fully water-saturated conditions. This study provides critical insights into the coupled transport processes of solutes in partially saturated clays.

1. Introduction

Clay-based materials, including compacted bentonite and clay rocks, are considered as buffer materials and host rocks for deep geological disposal of radioactive wastes due to their low permeability and swelling capacity. The porosity of clay-based materials consists of sub-micro to nanometer sized interparticle pores and sub-nanometer sized interlayer pores (Bourg et al., 2007). Radionuclide diffusion in these materials is influenced by various factors, such as the degree of water saturation (Gimmi & Churakov, 2019; Savoye et al., 2012), the pore size distributions of the clay-based materials, the salinity and composition of the pore solution (Glaus et al., 2020; Tachi & Yotsuji, 2014; Wigger & Van Loon, 2018), and/or size and shape of the clay particles (Tertre et al., 2018). Unsaturated conditions within the surrounding clay-based materials for long periods of time could be caused by the high temperature from decay heat and the hydrogen gas production from canister corrosion (Savoye et al., 2010). Significant gas production and heat generation might cause fractures in clay-based materials and eventually affect the long-term integrity of the multibarrier system (Tamayo-Mas et al., 2021). Therefore, understanding the mechanisms of solute transport through these clay-based materials under partially saturated conditions is critical for the evaluation of the long-term safety of geological repositories for radioactive wastes (Zheng et al., 2015).

In the past two decades, an extensive number of experiments (Gvirtzman & Gorelick, 1991; Revil & Jougnot, 2008; Savoye et al., 2010, 2012) provided in-depth insights into water and ion transport in unsaturated clay-based materials. As illustrated in Figure 1, at the scale of nanometers, the clay minerals can absorb water molecules by intermolecular adsorptive forces and generate a thin water film on their surface due to its hydrophilic nature (Nishiyama & Yokoyama, 2021). Hence, a thin water film covers the surfaces of partially saturated clays. The charged surfaces of clay minerals induce an electrical double layer (EDL) in the electrolyte solution, which influences the ion distribution within nanopores due to the long-range Coulomb force (Duncan, 1992; Yang &

© 2024. The Authors.

This is an open access article under the terms of the [Creative Commons Attribution-NonCommercial-NoDerivs License](https://creativecommons.org/licenses/by-nc-nd/4.0/), which permits use and distribution in any medium, provided the original work is properly cited, the use is non-commercial and no modifications or adaptations are made.

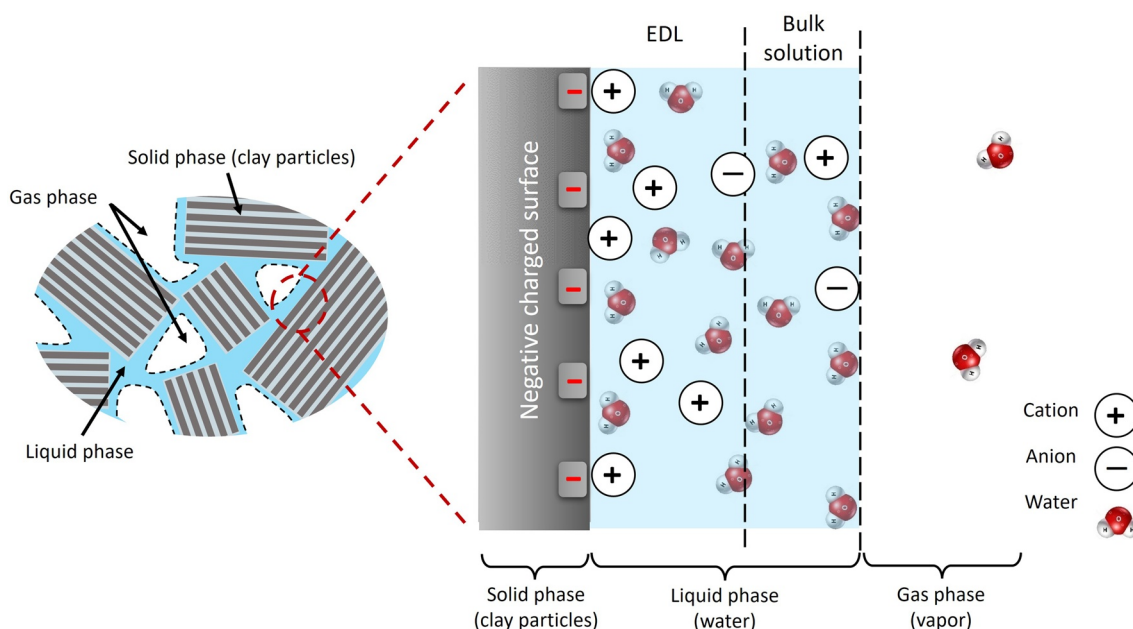


Figure 1. Sketch of the electrical double layer (EDL) within a nanoscale water film and the corresponding distributions of ions and water molecules in liquid and gas phases.

Wang, 2019). Thus, cations accumulate near negatively charged surfaces, while anions are excluded. In small nanometer sized pores, the EDL effect becomes very strong, and the assumption of electroneutrality of the entire pore solution is no longer appropriate (Miller & Wang, 2012). Experiments performed by Savoye et al. (2014) have shown that the effective diffusion coefficients of anions at trace concentrations in Callovo-Oxfordian claystones under variable water saturation are much smaller than that of tritiated water (HTO) or cesium ions, since the mean pore size of Callovo-Oxfordian claystones is comparable to the EDL thickness. Ion transport also alters the local composition of the pore solution, including pH and salinity, leading to changes in surface charge properties (Mullet et al., 1997; Sondi et al., 1996) and surface reactivity (Zhang & Wang, 2015), which in turn have an impact on ion transport. In addition, as anions are typically more polarizable than cations, they are located closer to the water-vapor interface than cations (Jungwirth & Tobias, 2002; Olivieri et al., 2018). As the thickness of the water film on solid surfaces approaches the nanometer scale, both the liquid-gas and liquid-solid interfaces may significantly affect ion distribution and further impact ion transport (cf. Figure 1). An additional challenge is the diffusion of volatile species, such as HTO or dissolved ^{14}C -bearing inorganic and organic compounds, in partially saturated clay-based materials. Compared with non-volatile tracers (i.e., ions), volatile species can diffuse across the liquid-gas interface, resulting in a different relationship between effective diffusion coefficient and saturation for volatile and non-volatile tracers (Savoye et al., 2010). Wang et al. (2022) recently observed experimentally that the effective diffusion coefficients of non-volatile $^{22}\text{Na}^+$ and $^{125}\text{I}^-$ tracers in compacted kaolinite decrease more rapidly than that of volatile HTO as the water saturation decreases.

Various efforts have been taken to achieve a model-based understanding of ion transport phenomena across various scales from molecular modeling (Churakov, 2013; Le Crom et al., 2021) to pore-scale simulations (Gimmi & Churakov, 2019), and continuum-scale models (Appelo et al., 2010; Muniruzzaman & Rolle, 2019; Revil & Jougnot, 2008). For example, Le Crom et al. (2021) simulated the processes of water desaturation and ion diffusion in a single interlayer pore at the atomic scale, which revealed a complex relationship of the average diffusion coefficient of water molecules and ions with respect to the water saturation. These molecular simulations provided more precise density distributions of ions and water and a more fundamental understanding of the water-vapor and water-solid interfacial effects on solute transport in nanopores. Underwood and Bourg (2020) carried out large-scale molecular dynamics (MD) simulations to study ion diffusion in compacted clay nanoparticles under fully water-saturated conditions. Since the computing cost of MD simulations in such three-dimensional (3D) nanostructures is extremely large, the derivation of transport parameters from atomistic simulations of realistic 3D nanostructures is still a challenge. Continuum-scale models are more computationally

efficient and straightforward to implement. However, these models require empirical or fitting geometry factors to consider the complexity of the unsaturated 3D pore network, such as tortuosity or connectivity (Gimmi & Alt-Epping, 2018; Soler et al., 2019). Furthermore, continuum-scale models utilize either the classical one-dimensional Poisson-Boltzmann model (Tournassat et al., 2009) or the Donnan model (Birgersson, 2017; Gimmi & Alt-Epping, 2018; Revil et al., 2011) to account for the influence of the EDL on the transport of charged species. The EDL may completely or partially overlap within the nanopores when the ionic strength is low, which may augment its influence (Miller & Wang, 2012; Tinnacher et al., 2016), where the Donnan model becomes inaccurate (Hsiao & Hedström, 2015; Yang & Wang, 2019). In case compacted clay-based materials are not fully water saturated, the coupling of the water/vapor interfacial effect with the EDL effect makes the mechanism of solute transport even more complex.

Pore-scale modeling relies on model-based representations of solid and fluid filled domains in the porous media (derived either from simulations or measurements) and can be used to bridge the molecular models with continuum-scale models. For instance, by using the simplified profiles of density distributions and transport properties at water-vapor and water-solid interfaces from the molecular simulations, Gimmi and Churakov (2019) solved Fick's law at the pore scale to calculate the effective diffusion coefficients of anions in reconstructed 2D pore-networks of bentonite under different humidity conditions. Yang and Wang (2019) utilized more fundamental Poisson-Nernst-Planck equations to understand ion diffusion in 3D nanostructures of saturated compacted clays. The solute transport processes in partially water-saturated nanoporous materials across scales still an unresolved scientific challenge. These processes need to be further investigated to allow for a more realistic description of coupled transport processes in variably saturated clay-based materials. Therefore, in this study we developed a pore-scale model that accounts for the water distribution and the EDL effect in 3D nanostructures to enhance the understanding of coupled transport processes in partially saturated clay-based materials. This study employed idealized clayey nanoporous media but could be extended to other types of clays if an appropriate representation of pore structure is available. The simulations performed by the developed pore-scale model are in particular focused on two main objectives: (a) investigations of water tracers diffusion in partially saturated nanoscale porous media, and (b) assessment of the EDL role in the diffusion of cations (i.e., ^{22}Na) and anions (i.e., ^{125}I) at trace concentrations (10^{-7} mol/L) with respect to different water saturations, including interpretation and extrapolation of data from existing experiments in illite/sand mixtures (Savoye et al., 2014) and compacted sedimentary rocks (García-Gutiérrez et al., 2023).

2. Methods

This study extends our previous numerical framework for saturated porous media (Wu et al., 2020; Yang & Wang, 2019; Yuan et al., 2022) to partially saturated conditions by adding (a) the equilibrium water/vapor distribution in pore geometries; (b) a stable method to capture the water transport through the water/vapor interface; (c) the electrokinetic boundary condition of liquid/gas interfaces; and (d) the local solute mobility relating to the distance away from the solid/liquid interface. The commonly used numerical method for pore-scale simulations is the Lattice Boltzmann Method (LBM) benefitting from its efficient parallelization and flexible handling of various liquid-solid boundary conditions. Hence, LBM is employed in this work to simulate the water/vapor distribution and the diffusion process at the pore scale. Specifically, the Shan-Chen LBM was used to simulate the spontaneous phase separation and to build the liquid/gas distribution in complex 3D pore geometries (Section 2.1). Subsequently, Fick's law is numerically solved using LBM to simulate water diffusion, while the coupled Poisson-Nernst-Planck equations are solved to simulate ion diffusion (Section 2.2).

The nanostructures of compacted clays were generated using the quartet structure generation set (QSGS) method based on the stochastic growth theory developed by Wang et al. (2007). By adjusting the growth factors and seed distribution probabilities, this method allows to control the statistical properties of the reconstructed microstructures, with respect to porosity, specific surface area, and mean particle/pore size. The regenerated nanostructures are not absolutely the same as the real structures of clays. This method has been utilized in previous pore-scale studies on diffusion in compacted clays and is detailed *inter alia* in Wu et al. (2020) and Yang and Wang (2019). Savoye et al. (2014) measured the effective diffusion coefficients of HTO and iodide in variably water-saturated illite/sand mixtures that exhibited porosities ranging from 0.24 to 0.36; the specific surface area (SSA) of the solids was estimated to range from $50 \text{ m}^2/\text{g}$ to $80 \text{ m}^2/\text{g}$ (corresponding volume-specific surface area: $0.09 \text{ l}/\text{nm} - 0.15 \text{ l}/\text{nm}$). García-Gutiérrez et al. (2023) analyzed the diffusion of HTO and chloride ions in variably water-saturated compacted sedimentary rocks, with porosities from 0.03 to 0.35 and an estimated SSA around $13 \text{ m}^2/\text{g}$ ($0.03 \text{ l}/\text{nm}$). In this study it was assumed that the nanostructures of compacted clays at the representative

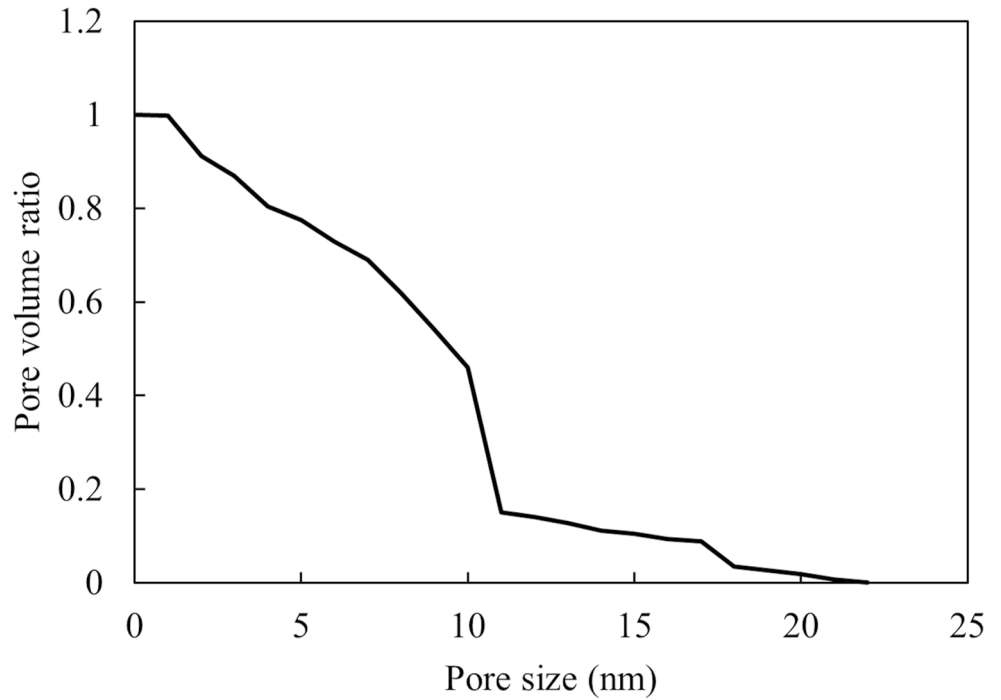


Figure 2. Pore size distribution of the regenerated clay.

elementary volume scale are isotropic and rigid. In order to compare with their experimental data, a clay that has similar structural characteristics (regarding porosity, mean pore size, and SSA) as the experimental samples was generated by utilizing the QSGS method. It is a $300 \times 300 \times 300$ nm cubic pore geometry of compacted clay with a resolution of 1 nm, with a porosity of 0.288 and a SSA of 0.106 1/nm (cf. Figure 6a). The pore size distribution of this regenerated clay is shown in Figure 2; the mean pore size is around 10 nm.

2.1. Evolution Equation of LBM for Phase Separation

The simulation of the static liquid-gas (water-vapor) distribution in the pore structures was performed using the two-phase single-component Shan-Chen LBM (Shan & Chen, 1993, 1994). Its evolution equation in the 3D nineteenth speed (D3Q19) lattice scheme is written as follows:

$$f_{\alpha}(\mathbf{r} + \mathbf{e}_{\alpha}\delta_x, t + \delta_t^f) - f_{\alpha}(\mathbf{r}, t) = -\frac{\delta_t^f}{\tau_f} [f_{\alpha}(\mathbf{r}, t) - f_{\alpha}^{\text{eq}}(\mathbf{r}, t)], \quad (1)$$

where f_{α} , \mathbf{r} , t , δ_x , δ_t^f , \mathbf{e}_{α} , and τ_f represent the distribution function along the direction α , the position vector, time, the grid size, the time step for phase separation, the discrete velocities, and the dimensionless relation time for the phase separation, respectively. The equilibrium function $f_{\alpha}^{\text{eq}}(\mathbf{r}, t)$ is given by:

$$f_{\alpha}^{\text{eq}}(\mathbf{r}, t) = \omega_{\alpha}\rho \left[1 + 3\frac{\mathbf{e}_{\alpha}\mathbf{v}}{c_f} + 9\frac{(\mathbf{e}_{\alpha}\mathbf{v})^2}{2c_f^2} - 3\frac{\mathbf{v}^2}{2c_f^2} \right], \quad (2)$$

$$\text{and } \omega_{\alpha} = \begin{cases} \frac{1}{3} & \alpha = 0 \\ \frac{1}{18} & \alpha = 1 - 6 \\ \frac{1}{36} & \alpha = 7 - 18 \end{cases}, \quad (3)$$

where ω_{α} is the distribution factor, ρ the density of the fluid, and \mathbf{v} the velocity of the fluid defined by the equilibrium distribution function, which is different from the fluid velocity $\mathbf{u} = \mathbf{v} - \tau_f \mathbf{F}_v / \rho$ with an external volumetric force \mathbf{F}_v . For the D3Q19 lattice, the discretized directions of \mathbf{e}_{α} used here are the same as the ones from Huang

et al. (2015). ρ and \mathbf{v} can be determined by $\rho(\mathbf{r}, t) = \sum_{\alpha} f_{\alpha}(\mathbf{r}, t)$ and $\mathbf{v} = \sum_{\alpha} f_{\alpha}(\mathbf{r}, t) \mathbf{e}_{\alpha} / \rho$, respectively. The macroscopic kinematic viscosity ν is related to the relaxation time: $\nu = c_f^2 (\tau_f - \delta_t^f / 2) / 3$, where $c_f = \delta_x / \delta_t^f$. The phase change is achieved via a volumetric interaction force, which is mathematically expressed as:

$$\mathbf{F}_V(\mathbf{r}, t) = -G\Phi(\mathbf{r}, t) \sum_{\alpha} \frac{\omega_{\alpha} \Phi(\mathbf{r} + \mathbf{e}_{\alpha} \delta_x, t) \mathbf{e}_{\alpha} c_f}{\sqrt{3}}, \quad (4)$$

and

$$\Phi(\mathbf{r}, t) = \Phi_0 \exp[-\rho_0 / \rho(\mathbf{r}, t)], \quad (5)$$

where Φ denotes the interaction potential and G the interaction strength, taken as -120 in arbitrary non-dimensional lattice units. $\Phi_0 = 4$ and $\rho_0 = 200$ are arbitrary constants. This study considers a set of parameters, where the densities of the gas phase and the aqueous phase are approximately $\rho_g = 85.86$ and $\rho_w = 527.98$ in arbitrary dimensionless lattice units, respectively, with a density ratio between the two phases of around 6. This density ratio is lower than the expected value, but it does not significantly affect the water/vapor distributions in rigid porous media, such as hardened cement paste (Bentz et al., 2022). A perfectly wetting solid boundary condition is assumed for water. The solid phase is assigned a pseudo density of the water phase for computing the volumetric interaction force (Bentz et al., 2022). This LBM for phase separation is similar to that developed by Xu et al. (2020). Furthermore, a bounce-back boundary condition is applied at the solid-liquid interface. To achieve the water distribution with a chosen volumetric water saturation S_w , an equilibrium distribution function with a density of $\rho(\mathbf{r}, 0) = (1 - S_w)\rho_g + S_w\rho_w$ and a zero-velocity fluid are used as initial conditions. After reaching a steady state, the liquid and gas phases can be separated by using a threshold density $\rho = 0.5\rho_g + 0.5\rho_w$. Voxels with densities lower than the threshold density are considered gas voxels, and those with densities above it are considered fluid voxels. The deformation will be significant in clays with drying to a low saturation level (Bag & Jadda, 2021) and the assumption of a rigid clay structure may fail. Hence, the minimal water saturation employed in this work is above 0.5 to reduce this hydromechanical effect. The Yantra open-source code (Patel, 2018) was used to implement the described model for phase separation.

2.2. Pore-Scale Modeling of Solute Transport

2.2.1. Governing Equation and Boundary Conditions

Solute transport in compacted clays is usually dominated by diffusion due to their ultra-low permeability. The impact of the EDL on ion diffusion in such clays has already been highlighted in the introduction. By treating ions as point charges with consideration of the EDL effect, the coupled Poisson-Nernst-Planck (PNP) model is utilized herein, in which the electrostatic potential field ψ is solved by the Poisson equation and the concentration distribution of the i th species C_i is solved by the Nernst-Planck equation (Probstein, 2005):

$$\frac{\partial C_i}{\partial t} = \nabla \cdot \left(D_i \nabla C_i + D_i \frac{z_i e C_i}{k_B T} \nabla \psi \right), \quad (6)$$

$$\nabla^2 \psi = - \sum_i \frac{z_i e N_A C_i}{\epsilon_r \epsilon_0}, \quad (7)$$

where D_i , z_i , t , e , k_B , T , N_A , and $\epsilon_r \epsilon_0$ denote the diffusion coefficient, the charge of the i th species, the time, the absolute charge of an electron (1.6×10^{-19} C), the Boltzmann constant (1.38×10^{-23} J/K), temperature, Avogadro's number (6.02×10^{23} 1/mol), and the permittivity of the pore solution, respectively. This study employs two different sets of the local diffusion coefficients D_i : identical diffusion coefficients $D_i = D_0$, and $D_i = D(x)$, which varies depending on the distance to solid surfaces (refer to Section 2.3 for more details). In the case of a dilute electrolyte, the distribution of ions as a function of distance from the clay surface follows the Maxwell-Boltzmann distribution:

$$C_i = C_{i,0} \exp\left(-\frac{z_i e \psi}{k_B T}\right), \quad (8)$$

with the bulk concentration $C_{i,0}$ at an infinite distance from the surface. Hence, by substituting Equation 8 into Equation 7, we get the Poisson-Boltzmann equation:

$$\nabla^2 \psi = - \sum_i \frac{z_i e N_A C_{i,0}}{\epsilon_r \epsilon_0} \exp\left(-\frac{z_i e \psi}{k_B T}\right). \quad (9)$$

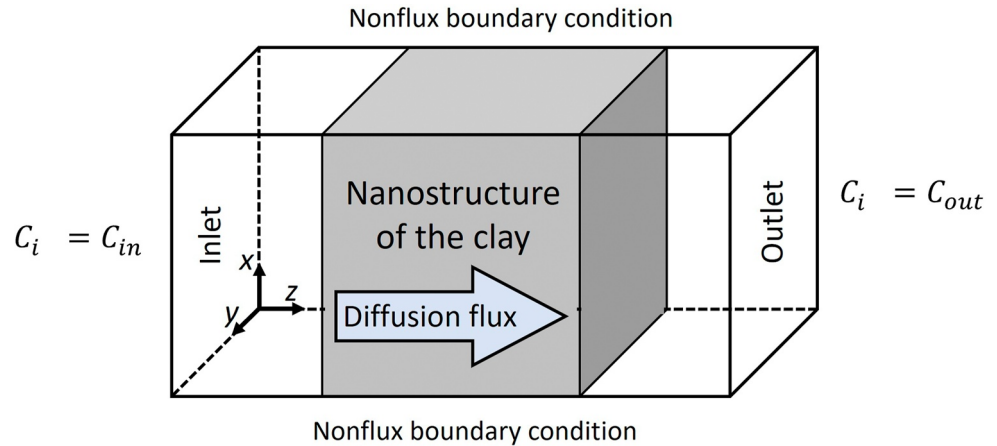


Figure 3. Schematic overview of the 3D simulation domain and boundary conditions.

Equations 6 and 9 are the Poisson-Boltzmann-Nernst-Planck equations governing the solute transport process in the complex pore geometries of compacted clays. For non-charged solutes, like water molecules, the PNP model reduces to the classical Fick's equation:

$$\frac{\partial C}{\partial t} = \nabla \cdot (D \nabla C). \quad (10)$$

In the 3D simulations, constant concentration conditions of charged tracers (i.e., ^{22}Na and ^{125}I) are used at the inlet and outlet $C_i = C_{in,i}$ or $C_{out,i}$, while a nonflux boundary condition is used on other surfaces of the simulation domain (Figure 3). The ion transport is limited to the liquid phase, while water molecules can access both the gas and liquid phase. Therefore, the nonflux boundary condition is applied for ions at liquid-solid and liquid-gas interfaces, while water molecules use this boundary condition at liquid-solid and gas-solid interfaces. A zero electrical potential $\psi = 0$ V is applied at the inlet and outlet and a zero gradient of electrical potential $\partial\psi/\partial x = 0$ V/m on other boundaries of the simulation domain. A constant surface charge density σ_0 at the clay surface is adopted as the boundary condition for the Poisson equation $\nabla\psi|_{\text{surface}} = -\sigma_0/(\epsilon_r\epsilon_0)$. The electrokinetic property at the liquid/gas interface under nanoconfined conditions is still debated (Bjorneholm et al., 2016; Levin et al., 2009; Olivieri et al., 2018). Previous studies suggested that the liquid/gas interface is also a charged interface but its surface charge density is negligible compared to that of clay surfaces (Leroy et al., 2012; Revil et al., 2007). Hence, this study assumes a zero surface charge density at the liquid/gas interface. For the initialization of simulations, $C_i = C_{out,i}$ and $\psi = 0$ are applied as the initial conditions. Room temperature (298 K) is applied for all simulations. Under steady-state conditions, the effective diffusion coefficient is calculated by the flux J_i of the i th solute per unit cross-section:

$$D_e = \frac{J_i \cdot L}{C_{in} - C_{out}}, \quad (11)$$

where L is the length of the domain along the transport direction. To avoid the influence of the transition regions on the computation of effective diffusion coefficient of HTO, the inlet concentration, C_{in} in Equation 11, is defined here as the mean concentration of HTO on the left side of the clay, while the outlet concentration, C_{out} , is defined as the mean concentration of HTO on the right side of the clay. To eliminate this influence on the D_e^* of the ions, the inlet and outlet concentrations in Equation 11 were defined by the following formulas based on the Maxwell-Boltzmann distribution:

$$C_{i,\text{in}} = \bar{C}_i^{\text{left}} \exp\left(\frac{z_i e \bar{\psi}^{\text{left}}}{k_B T}\right), \quad (12)$$

$$C_{i,\text{out}} = \bar{C}_i^{\text{right}} \exp\left(\frac{z_i e \bar{\psi}^{\text{right}}}{k_B T}\right), \quad (13)$$

where \bar{C}_i^{left} , $\bar{\psi}^{\text{left}}$, \bar{C}_i^{right} , and $\bar{\psi}^{\text{right}}$ are the mean concentration of ions and electrical potential on the left side of the clay, as well as the mean concentration and electrical potential on the right side of the clay, respectively.

2.2.2. Corresponding Evolution Equations of LBM

The 3D coupled Equations 6 and 9, subjected to the appropriate boundary conditions, are numerically solved by previously developed GPU-LBM codes (Yang & Wang, 2018b, 2019). The D3Q7 lattice system is proven to be very stable and robust for solving the PNP model (Yang & Wang, 2018a). Besides, it also has a higher efficiency compared to higher-order lattice schemes. In a D3Q7 lattice system of single-relaxation-time LBM, the evolution equation g_α^i for the i th solute transport along the direction α (cf. Equation 6) is:

$$g_\alpha^i(\mathbf{r} + \mathbf{e}_\alpha \delta_x, t + \delta_t) - g_\alpha^i(\mathbf{r}, t) = -\frac{1}{\tau_{D_i(\mathbf{r})}} [g_\alpha^i(\mathbf{r}, t) - g_\alpha^{i,\text{eq}}(\mathbf{r}, t)], \quad (14)$$

where δ_t and $\tau_{D_i(\mathbf{r})}$ denote the time step and the dimensionless relaxation time for the solute transport related to the diffusion coefficient $D_i(\mathbf{r})$. The value of $\tau_{D_i(\mathbf{r})}$ in each grid is determined through the local diffusion coefficient $D_i(\mathbf{r})$ by the following equation:

$$\tau_{D_i(\mathbf{r})} = \frac{4D_i(\mathbf{r})}{c_g \delta_x} + \frac{1}{2}. \quad (15)$$

Here, c_g represents the diffusion lattice speed defined as $c_g = \delta_x / \delta_t$. For numerical stability considerations, it is recommended to confine $\tau_{D_i(\mathbf{r})}$ within the range of 0.5–2, that is, $\tau_{D_i(\mathbf{r})} \in (0.5, 2)$. \mathbf{e}_α denotes the discrete velocities, where $\alpha = 0, 1, \dots, 6$ representing the discretized directions as in Yang and Wang (2018b). The equilibrium distribution function $g_\alpha^{i,\text{eq}}(\mathbf{r}, t)$ is given by:

$$g_\alpha^{i,\text{eq}}(\mathbf{r}, t) = \omega_\alpha C_i \left[1 - 4D_i(\mathbf{r}) \frac{e_{z_i} \mathbf{e}_\alpha}{c_g k_B T} \nabla \psi \right], \quad (16)$$

with

$$\omega_\alpha = \begin{cases} \frac{1}{4} & \alpha = 0 \\ \frac{1}{8} & \alpha = 1 - 6 \end{cases}. \quad (17)$$

The evolution equation on the same set of lattices for the Poisson-Boltzmann equation (cf. Equation 9) is:

$$h_\alpha(\mathbf{r} + \mathbf{e}_\alpha \delta_x, t + \delta_{t,h}) - h_\alpha(\mathbf{r}, t) = -\frac{1}{\tau_h} [h_\alpha(\mathbf{r}, t) - h_\alpha^{\text{eq}}(\mathbf{r}, t)] + \sum_i \frac{\omega_\alpha \delta_{t,h} e N_A z_i C_{i,0}}{\epsilon_r \epsilon_0} \exp\left(-\frac{z_i e \psi}{k_B T}\right), \quad (18)$$

where $\delta_{t,h}$ is the time step for h_α evolution and $\tau_h = 4\delta_{t,h} / \delta_x^2 + 0.5$ is the corresponding dimensionless relaxation time. The equilibrium distribution function $h_\alpha^{\text{eq}}(\mathbf{r}, t)$ is written as:

$$h_\alpha^{\text{eq}}(\mathbf{r}, t) = \omega_\alpha \psi. \quad (19)$$

The gradient of ψ along the j direction $\partial\psi/\partial x_j$ can be calculated by $\partial\psi/\partial x_j = -4\sum_\alpha (\mathbf{e}_j \cdot \mathbf{e}_\alpha) h_\alpha / (\tau_h \delta_x)$ with a unit vector \mathbf{e}_j . The concentration and electrical potential on each grid are then calculated respectively as $C_i(\mathbf{r}, t) = \sum_\alpha g_\alpha^i(\mathbf{r}, t)$ and $\psi(\mathbf{r}, t) = \sum_\alpha h_\alpha(\mathbf{r}, t)$. Using the boundary conditions described above, it was proved that the evolution equations can recover the governing Equations 6 and 9 through the Chapman-Enskog expansion. In the LBM scheme, the local flux of solutes can be easily obtained by the distribution functions: $J_i(\mathbf{r}, t) \cdot \mathbf{e}_j = [(\tau_{D_i(\mathbf{r})} - 0.5) / \tau_{D_i(\mathbf{r})} c_g] \sum_\alpha (\mathbf{e}_j \cdot \mathbf{e}_\alpha) g_\alpha^i(\mathbf{r}, t)$. The classical bounce-back rule is employed as the nonflux boundary condition for solute transport and the zero-gradient boundary condition for the Poisson equation. The Dirichlet boundary condition for solute transport $C_i = C_{0,i}$ is $g_\alpha^i(\mathbf{r}, t + \delta_t) = -g_\beta^i(\mathbf{r}, t) + 0.25C_{0,i}$ and that for Poisson equation ($\psi = 0$ V) is $h_\alpha(\mathbf{r}, t + \delta_t) = -h_\beta(\mathbf{r}, t)$, where index α and β are the opposite directions normal to the interface and β is the direction toward the surface. The Neumann boundary condition for the Poisson equation $\nabla\psi|_{\text{surface}} = -\sigma_0 / (\epsilon_r \epsilon_0)$ is obtained by: $h_\alpha(\mathbf{r}, t + \delta_t) = h_\beta(\mathbf{r}, t) + \sigma_0 \delta_{t,h} / (\epsilon_r \epsilon_0 \delta_x)$. The Poisson-Boltzmann equation (cf. Equation 9) is solved iteratively in the numerical scheme until the electrical potential converges, then the

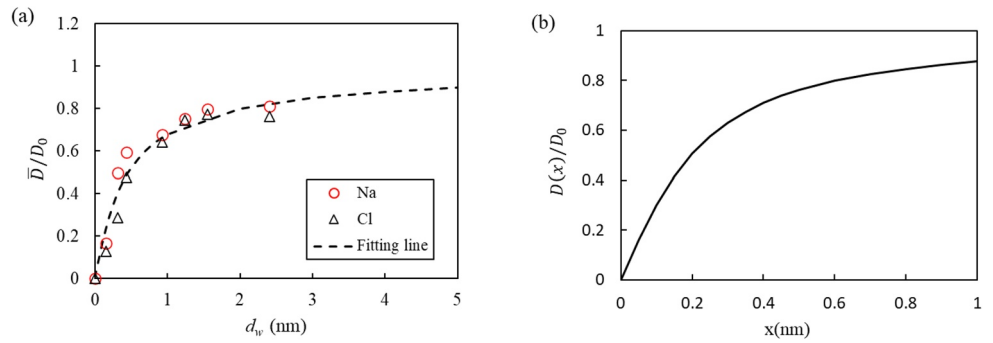


Figure 4. (a) $\bar{D}(d_w)/D_0$ values of Na^+ (red circles) and Cl^- (black triangles) obtained from the molecular simulations of Le Crom et al. (2021) and the fitting formula (black dashed line, cf. Equation 22); (b) dimensionless diffusion coefficient $D(x)/D_0$ as function of the distance to the clay mineral surface x for $a = 5.3$ (cf. Equation 20).

evolutions of solutes are numerically solved to reach a steady state. The detailed procedure can be found in our previous studies (Yang & Wang, 2018b, 2019). This numerical framework for solute transport in fully saturated porous media has already been validated in our previous work (Tian et al., 2015; Yang & Wang, 2018a), which indicates that the accuracy and robustness of our framework are suitable to capture interactions between ions and charged surfaces.

2.3. Relationship of Solute Mobility With Distance to the Solid Surface

Several molecular studies indicated a nonlinear decrease of solute mobility or diffusion coefficient in close proximity to clay mineral surfaces caused by water structuring and preferential interaction with the surface (Churakov, 2013; Le Crom et al., 2021), while the diffusivity in domains more than three molecular diameters of the water molecule away from the surface is expected to be equal to the diffusion coefficient in bulk water D_0 . Therefore, the diffusion coefficient $D(x)$ as a function of the distance from the clay mineral surface x is proposed to be:

$$D(x) = \frac{2D_0 \arctan(ax)}{\pi}, \quad (20)$$

including a decay parameter a . This parameter can be calculated by fitting the results from molecular simulations. The average diffusion coefficient within a water film of a thickness d_w is determined by:

$$\bar{D}(d_w) = \frac{1}{d_w} \int_0^{d_w} D(x) dx, \quad (21)$$

Substituting Equation 20 into Equation 21 yields:

$$\frac{\bar{D}(d_w)}{D_0} = \frac{d_w \arctan(ad_w) - 0.5 \ln(a^2 x d_w^2 + 1)/d_w}{1.57 d_w}. \quad (22)$$

The crosses presented in Figure 4a are $\bar{D}(d_w)/D_0$ values of sodium and chloride ions obtained from previous molecular simulations by Le Crom et al. (2021). It can be observed that the $\bar{D}(d_w)/D_0$ curves for sodium and chloride ions are similar. However, the substantial difference in diffusion coefficient of water molecules between the liquid and gas phases may affect the $\bar{D}(d_w)/D_0$ value under unsaturated conditions. For simplification, we assume that the $\bar{D}(d_w)/D_0$ dependence for water molecules within the liquid phase is identical to that of the ions. Finally, by fitting with these data, the parameter $a = 5.3$ 1/nm is derived. The black dashed line in Figure 4a is the fitting curve of $\bar{D}(d_w)/D_0$ and the line in Figure 4b represents the dimensionless diffusion coefficient $D(x)/D_0$ for solutes with respect to the distance x . The different force fields employed in the molecular simulations could change the value of a , but this influence is ignorable on D_e since the most of the pores in the regenerated clay are larger than 5 nm (cf. Figure 2).

2.4. Transport of Water Molecules Through the Liquid/Gas Interface

Henry's Law states that the concentration of a volatile species in a liquid is directly proportional to its partial pressure in the gas phase. The dimensionless Henry solubility coefficient (He) represents the equilibrium solubility of a volatile

species in a liquid, expressed as the ratio between its concentration (C_l) in the aqueous phase and its concentration (C_g) in the gas phase (Sander, 2015). At the liquid/gas interface Γ , the mass flux of the volatile species is conserved, but its concentration exhibits a sharp drop governed by Henry's law (Lu et al., 2019; Sander, 2015). By assuming that the accommodation coefficient of water equals unity at room temperature (Viecelli et al., 2004), we get:

$$-D_g \nabla C_g \Big|_{\Gamma} = -D_l \nabla C_l \Big|_{\Gamma}, \quad (23)$$

with

$$He = \frac{C_l}{C_g} \Big|_{\Gamma}, \quad (24)$$

where the diffusion coefficients of a volatile species are D_l in the liquid phase and D_g in the gas phase, respectively. The presence of discontinuities in concentration and diffusion coefficient at the interface often results in a numerical instability of LBM. Numerically solving the volatile solute diffusion across the liquid/gas interface is a challenge due to the significant differences in concentration and diffusion coefficient between the liquid and gas phases. Specifically, simulating the transfer of volatile HTO with a remarkably large Henry solubility coefficient poses a significant challenge. To avoid sharp jumps in concentration and diffusion coefficient at the interface, this study hypothesizes an equivalent solute C^e subject to the following constraints:

$$C_g^e = C_g He, \quad (25)$$

$$C_l^e = C_l, \quad (26)$$

$$D_l^e = D_l, \quad (27)$$

and

$$D_g^e = D_g / He, \quad (28)$$

where C_g^e , C_l^e , D_l^e , and D_g^e denote the concentrations and diffusion coefficients of the equivalent solute species in the gas phase and liquid phase, respectively. Substituting Equations 25–28 into Equations 23 and 24, we can finally get:

$$-D_g^e \nabla C_g^e \Big|_{\Gamma} = -D_l^e \nabla C_l^e \Big|_{\Gamma}, \quad (29)$$

$$C_g^e \Big|_{\Gamma} = C_l^e \Big|_{\Gamma}. \quad (30)$$

The hypothesized solute species satisfies both the mass flux and concentration continuities at the interface while avoiding a sharp concentration jump at the steady state. This approach for water tracers is not validated for the unsteady state because it does not consider the evaporation/condensation rate through the liquid/gas interface. Additionally, the difference in diffusion coefficients at the interface also decreases for some volatile solutes by using this approach. For example, the transport parameters for HTO are $D_l = 2 \times 10^{-9}$ m²/s, $D_g = 2.6 \times 10^{-5}$ m²/s, and $He = 6.0 \times 10^4$ at room temperature (298 K) and 1013.25 hPa (Wang et al., 2022). It is important to note that He of HTO can be affected by other factors such as the ionic strength of the solution. Since this study addresses dilute electrolytes, He in the electrolyte is assumed to be identical to He in free water. While the real diffusion coefficient ratio of HTO is $D_g/D_l = 1.3 \times 10^4$, the corresponding ratio for its equivalent solute is only $D_g^e/D_l^e = D_g/(He \cdot D_l) = 0.22$. It is also very easy to obtain the actual concentration distribution from that of the equivalent solute by using Equation 25. Therefore, this approach greatly improves the stability of the LBM simulations.

2.5. Adsorption of Thin Water Films on Clay Surfaces

At the molecular scale, the intermolecular adsorptive forces can lead to a thin water film on the clay surface due to its hydrophilic nature. The thickness of the water film is influenced by changes in relative humidity and temperature (Leão & Tuller, 2014), as well as by the types of clay minerals and electrolytes present (Gimmi & Churakov, 2019). Molecular simulations by Gimmi and Churakov (2019) investigated the thickness of water films on different surfaces of montmorillonite. Their simulations showed that the thickness of the water films on

Table 1
Parameters Used in 1D Steady State Transfer of HTO Between Liquid and Gas Phase

Geometry and mesh	
Physical length H (μm)	1
Number of grids used in LBM	100
Transport parameters	
Concentration boundary at the liquid side C_{lb} (mol/L)	1
Concentration boundary at the gas side C_{gb} (mol/L)	0
Diffusion coefficient in the liquid phase $D_{l,0}$ (m^2/s)	2.0×10^{-9}
Diffusion coefficient in the gas phase $D_{g,0}$ (m^2/s)	2.6×10^{-5}
Dimensionless Henry solubility coefficient He	6.0×10^4

the external clay surface ranged from 0.3 to 2.95 nm as the relative humidity changed from 43% to 94%. However, for the sake of simplicity, this study considers two fixed thicknesses of water films: 0 nm (i.e., ignoring the water film) and 1 nm. After performing the phase separation simulation by the LBM (described in Section 2.1), the water-film grids replace the gas grids near the gas/solid interface based on the water-film thickness. Herein, the water-film grids are assumed to have identical properties (e.g., with respect to diffusion coefficients) as the liquid grids.

3. Results and Discussions

3.1. Water Diffusion in Partially Saturated Porous Media

3.1.1. 1D Steady State Transfer Between Liquid and Gas Phase

A one-dimensional example of steady state HTO transfer between liquid phase and gas phase is considered to test the methodology described in Section 2.4. The computational domain has a length of $H = 1 \mu\text{m}$, and the liquid/air interface is positioned at the midpoint. The left side is the liquid phase, and the right side is the gas phase. A constant concentration boundary condition is used on both sides ($C_{lb} = 1 \text{ mol/L}$, $C_{gb} = 0 \text{ mol/L}$). All parameters used in this benchmark are tabulated in Table 1. At steady state, the analytical solution for the concentration distribution is (Lu et al., 2019):

$$C(x) = \begin{cases} \frac{D_g C_{gb} - D_g H e C_{lb}}{D_l + D_g H e} \frac{2x}{H} + C_{lb} & x < \frac{H}{2} \\ \frac{D_l C_{gb} - D_l H e C_{lb}}{D_l + D_g H e} \frac{2x}{H} + \frac{D_g H e C_{gb} + 2D_l H e C_{lb} - D_l C_{gb}}{D_l + D_g H e} & x \geq \frac{H}{2} \end{cases} \quad (9)$$

Figure 5 shows the concentration distribution of HTO in this one-dimensional example. Notably, a sharp concentration jump is observed at the liquid/gas interface. Remarkably, to directly simulate the diffusion within a region with a sharp concentration and diffusion coefficient jump is a big challenge for the classical single-relaxation-time LBM (Perko & Patel, 2014). However, the simulation exhibits a good agreement with the analytical solution, thereby validating the method developed in Section 2.4. After this validation, our method can be used to simulate HTO diffusion in unsaturated compacted clays.

3.1.2. 3D Steady State Diffusion in Compacted Clays

This section describes the simulations of water diffusion in unsaturated compacted clays. The grid size of the LBM used is identical to the resolution of the regenerated nanostructure of the clay. Various water saturations ranging from 0.5 to 1 were set in the compacted clay by the LBM described in Section 2.1. In the simulation domain for HTO transport, two transition regions are connected with the inlet and outlet sides of the compacted clays, consistent with our previous studies (Yang & Wang, 2018b, 2019). The simulation domain and the corresponding boundary conditions are schematically illustrated in Figure 3. An overview of the mesh discretization and simulation parameters is tabulated in Table 2. After the diffusion reaches steady state by solving Fick's law (cf. Equation 10) and using the developed equivalent solute method (cf. Section 2.4), the effective diffusion coefficients can be calculated by Equation 11. Figures 6a–6d present two simulated examples of 3D phase distribution and tracer concentration distribution in the nanostructure at saturation levels of 1.0 (i.e., full saturation) and 0.73, respectively. Focusing on one single pore shown in the black square of Figure 6c, the local diffusion coefficient and concentration distributions along the red line are determined as shown in Figure 6e. Here, the local diffusion coefficient within the liquid phase decreases near the clay surface which follows from Equation 20. Besides, our model accurately captures the sharp jump in the HTO concentration near the liquid/gas interface governed by Henry's law, which approves, again, the stability and accuracy of the developed equivalent solute method.

Four scenarios for the simulation of HTO diffusion are examined here: (a) employing a constant diffusion coefficient, $D_{l,0}$, in the liquid phase without the presence of thin water films on the clay surface (cf. case 1 in Table 2); (b) employing a location-dependent diffusion coefficient (as outlined in Section 2.3) in the liquid phase without thin water films on the surface (case 2); (c) incorporating thin water films (as described in Section 2.5) while using a variable diffusion coefficient (case 3); and (d) evaluating the Knudsen effect and transport resistance at the interface (case 4). Figure 7 presents the relative effective diffusion coefficients D_e^* as a function of water

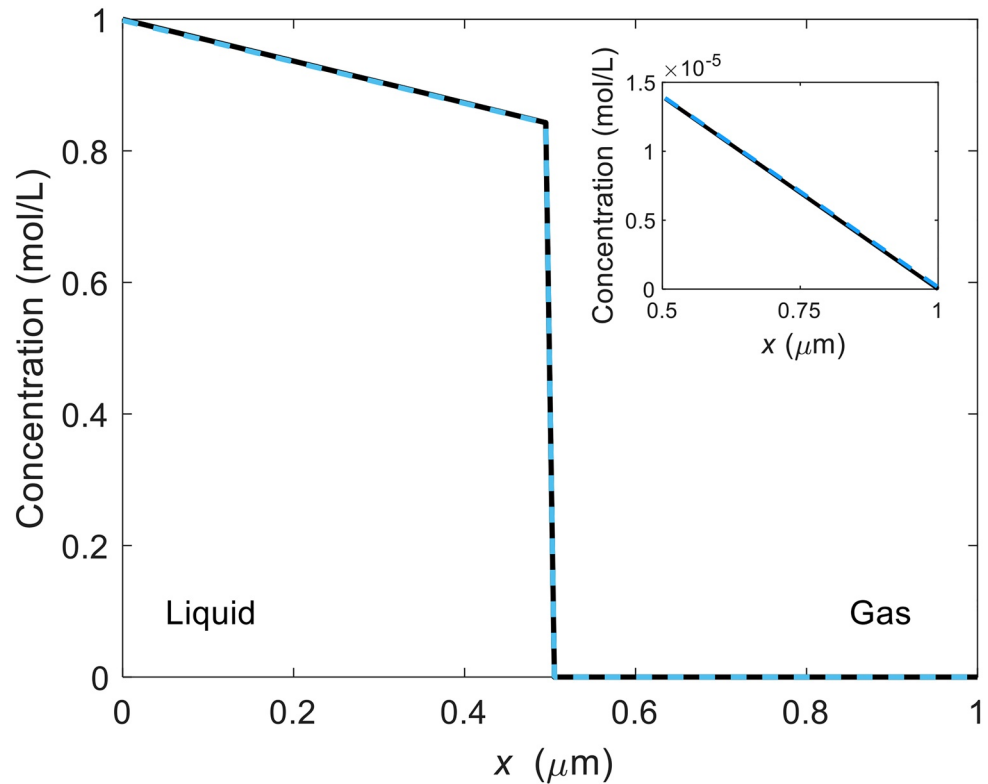


Figure 5. Concentration distribution of 1D steady transfer of HTO between liquid and gas phases as given by our model (blue line) compared to the analytical solution (black dashed line, cf. Equation 31).

saturation determined by our pore-scale model. In all cases, D_c^* decreases with decreasing degree of water saturation. Compared to the D_c^* calculated by using a constant diffusion coefficient (case 1), utilizing a variable local diffusion coefficient (case 2) results in a decrease in D_c^* of approximately 7% at saturation levels ranging from 0.55 to 1.0. This indicates that the liquid phase is the primary medium for HTO tracer diffusion. At lower saturation levels, HTO diffusion becomes slightly more sensitive to the diffusion coefficient $D(r)$ near the clay surface. For example, in fully saturated conditions, the relative difference with and without utilizing the changed local diffusion coefficient is 6.9% whereas this difference slightly increases to 7.4% as the saturation decreases to 0.54. Involving the thin nanoscale water film leads to an increase of approximately 11% in D_c^* because the surface water films create a diffusive pathway in the pores clogged by the gas phase. The simulation results reveal that the impact of water films on HTO diffusion increases at lower water saturation, in line with previous investigations (Tokunaga et al., 2017). Thus these surface water films play a crucial role in enhancing HTO diffusion through the clay matrix at low water saturation.

Other effects, such as the Knudsen effect and the resistance of the liquid/gas interface, can also have an influence on HTO diffusion in partially saturated compacted clays. The Knudsen effect describes the confined gas diffusion in nanoscale pores whose size is comparable to the mean free path (MFP) of the gas molecules, where the collision between the gas molecule and solid or liquid surface is not negligible (Krishna & van Baten, 2012). At room temperature and atmospheric pressure, the MFP of HTO is around dozens of nanometers. According to the pore size distribution shown in Figure 2, the mean pore size of the generated clay is smaller than the MFP, and hence, Knudsen diffusion will play an important role in these nanoscale pores. The mean diffusion coefficient of HTO vapor in the nanoscale pores $D_{g,p}$ can be reduced by the Knudsen effect and its value is estimated by the empirical Bosanquet formula (Guo et al., 2018):

$$D_{g,p} = \frac{1}{1 + \frac{9}{5}Kn} D_{g,0}, \quad (32)$$

where the Knudsen number Kn is the ratio of the MFP and the mean pore size \bar{d} , $Kn = \text{MFP}/\bar{d}$.

Table 2
Overview of Parameters of the 3D Steady State Diffusion Simulation of HTO in a Compacted Clay

Geometry and mesh				
Porosity				0.288
Physical size (nm)				$300 \times 300 \times 300$
Physical size of one transition region				$300 \times 300 \times 30$
Water saturation				0.54; 0.64; 0.68; 0.73; 1.0
Number of grids used in LBM				
<i>x</i> -axis				300
<i>y</i> -axis				300
<i>z</i> -axis				360
Parameters in transport model				
$D_{l,0}$ (m ² /s)				2.0×10^{-9}
$D_{g,0}$ (m ² /s)				2.6×10^{-5}
<i>He</i>				6.0×10^4
Concentration boundary of the transition region at the inlet C_{in} (mol/L)				1.0×10^{-7}
Concentration boundary of the transition region at the outlet C_{out} (mol/L)				1.0×10^{-8}
Temperature <i>T</i> (K)				298
Simulation cases				
No.	1	2	3	4
Diffusion coefficient in the liquid phase $D(r)$	$D_{l,0}$	Equation 20	Equation 20	Equation 20
Thickness of water film (nm)	0	0	1	0
Diffusion coefficient in the gas phase	$D_{g,0}$	$D_{g,0}$	$D_{g,0}$	0

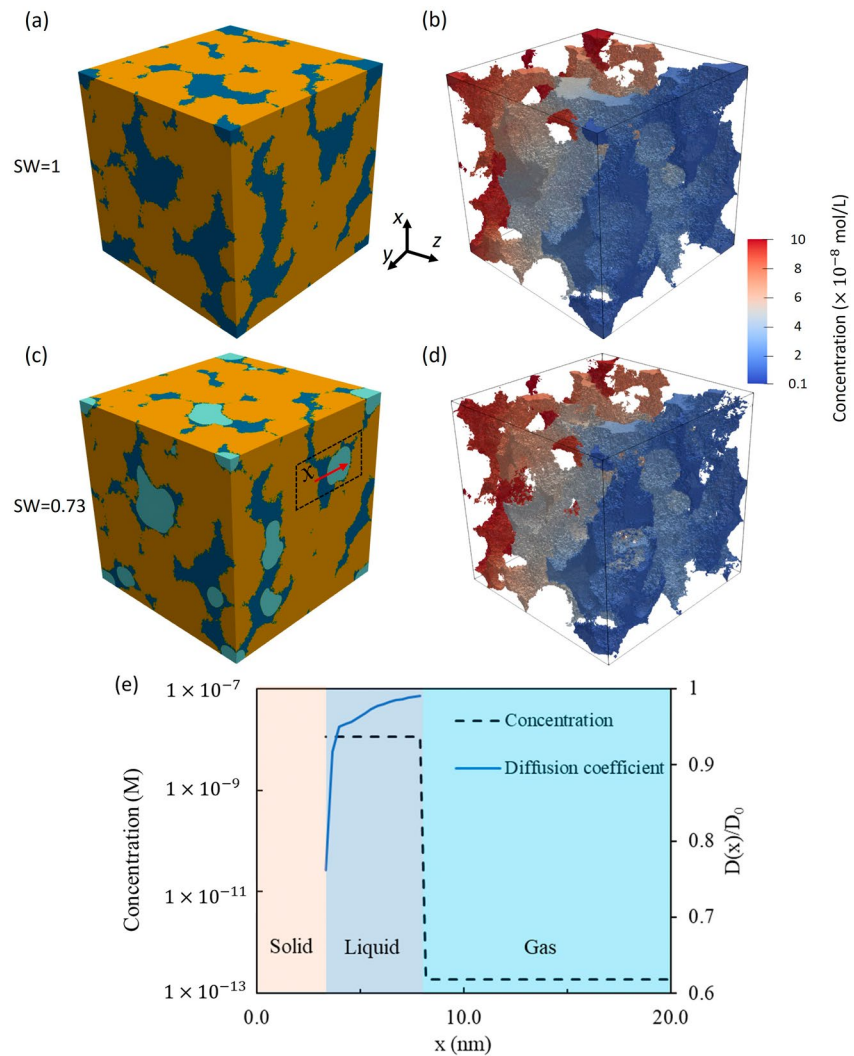


Figure 6. Phase (a, c) and HTO concentration (b, d) distributions in the nanostructure at water saturations of 1.0 (a, b) and 0.73 (c, d). In (a, b), the brown, dark blue and light blue phases represent the clay particles, the liquid and the gas phase, respectively. (b, d) only present the HTO concentration in the liquid phase. The local diffusion coefficient distribution in the liquid phase and HTO concentration distributions in both gas and liquid phases along the red line in (c) are shown in (e).

The other effect mentioned above, the transport resistance through the liquid/gas interface, has been observed in experiments (Lee et al., 2014). This resistance arises due to an accommodation coefficient of water below unity (Miles et al., 2012). At thermodynamic equilibrium, the flux of water molecules condensing into the liquid phase is equal to the flux of water molecules evaporating from the liquid phase. The resulting interface resistance can reduce the flux of HTO through the liquid/gas interface at the nanometer scale. In this study, Kn exhibits a range of approximately 2–20. This range of Kn values gives rise to a decrease in $D_{g,p}$, which spans from 0.03 to 0.22. As a consequence, D_g^e/D_l^e described in Section 2.4 is also significantly diminished. By incorporating the interface resistance, an asymptotic case is that diffusion in the gas phase is not taken into account $D_g^e/D_l^e \approx 0$, in which situation the migration of HTO can be assumed only to take place in the liquid phase (cf. case 4 in Table 2). The orange solid and dashed lines in Figure 7 compare the results of whether HTO is accessible into the gas phase under the same conditions. The simulation results show that this alteration has a critical effect on D_g^e of HTO. Assuming $D_g^e/D_l^e \approx 0$ results in an approximately 50% reduction in the value of D_g^e for HTO tracers when the saturation level decreases from 1.0 to 0.64. Gimmi and Churakov (2019) also simulated HTO diffusion by using $D_g^e/D_l^e = 0$ in a 2D unsaturated “CV-10” smectite. A similar trend was observed in 2D simulations by Gimmi and Churakov (2019) (cf. black dash-point line in Figure 7). The differences are related to the geometrical connectivity of the media and percolation threshold in 2D and 3D systems.

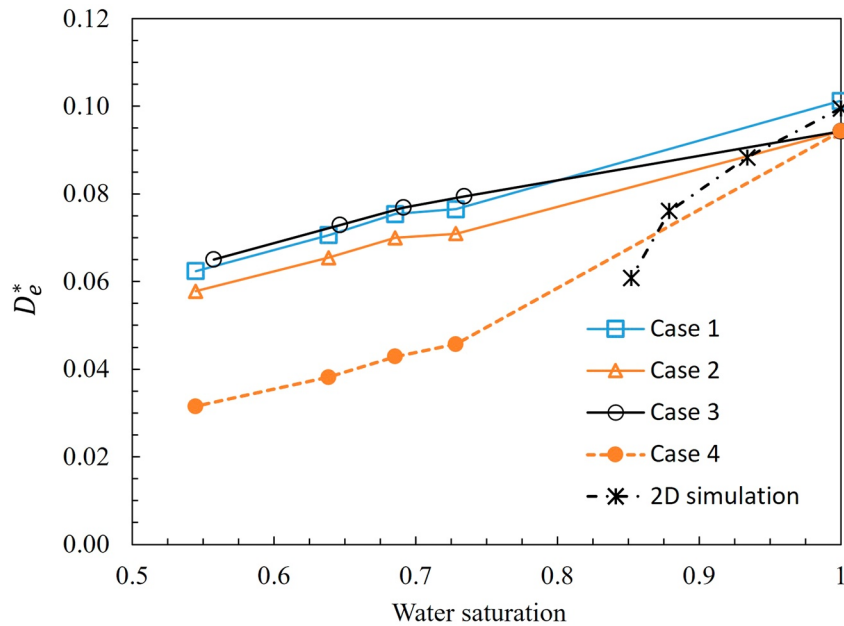


Figure 7. Simulated relative effective diffusion coefficients D_e^* of HTO in the nanostructure as function of water saturation. The blue solid line is simulated by using a constant diffusion coefficient (case 1); the orange solid line by a location-dependent diffusion coefficient (case 2); the black solid line by adding a 1 nm thin water film (case 3); and the orange dashed line by assuming $D_g^e/D_l^e \approx 0$ (case 4). The black dash-point line gives the results of 2D simulations of HTO diffusion in variably saturated smectite by Gimmi and Churakov (2019) for comparison.

3.2. Ion Diffusion in Partially Saturated Compacted Clays

The same clay nanostructure and liquid/gas distributions as those in Section 3.1 were used to investigate the diffusion of ions under unsaturated conditions. In this section, the same simulation domain and boundary conditions as above are also employed for the simulation of ion diffusion. A zero electrical potential is applied for the inlet and outlet $\psi_{\text{inlet/outlet}} = 0$ V and a $^{23}\text{NaCl}$ electrolyte is used as a pore solution. The effective diffusion coefficients of two tracers ^{22}Na and ^{125}I were simulated using the parameters summarized in Table 3. Previous studies (Birgersson, 2017; Van Schaik et al., 1966; Yang & Wang, 2019) indicated that the dimensionless normalized volume charge density ρ_e^* , the ratio of total carried charges between clay surface and pore solution, determines the strength of the EDL effect on ion diffusion in compacted clays. ρ_e^* is determined by:

$$\rho_e^* = \frac{\text{CEC}\rho_{bd}}{\varphi_w I_s} = -\frac{\sigma_0 \text{SSA}}{\varphi_w e N_A I_s}, \quad (33)$$

where CEC denotes the cation exchange capacity (equiv/kg), ρ_{bd} the dry density of the compacted clays (kg/m^3), and φ_w the water content. The water content φ_w is determined by using the porosity θ and water saturation S_e as: $\varphi_w = S_e \theta$. The ionic strength I_s is calculated as $I_s = 0.5 \sum z_i C_{i,0}$. The illite/sand mixtures used by Savoye et al. (2014) exhibited a CEC in the range of 0.1 equiv/kg to 0.2 equiv/kg, as well as ρ_{bd} ranging from 1760 kg/m^3 to 1840 kg/m^3 . The ionic strength I_s of their pore solution is 0.1 M, which yielded a ρ_e^* in their experiment around 8 in the saturated illite/sand mixtures. For the sedimentary rocks used by García-Gutiérrez et al. (2023), the estimated CEC is about 0.07 equiv/kg, ρ_{bd} around 1650 kg/m^3 , and $I_s = 0.027$ M, which gives a $\rho_e^* \sim 10$ at full water saturation. Our previous study (Yang & Wang, 2019) indicated that simulations with identical ρ_e^* could cause a similar EDL effect on ion diffusion. Therefore, to keep the ρ_e^* values of simulations close to those in the experiments, this study used a set of surface charge densities σ_0 and bulk concentrations $C_{i,0}$ tabulated in Table 3, and the resulting values of ρ_e^* ranged from 0.38 to 8 at full saturation. The thickness of EDL is the distance of the region away from the solid surface where $C_{\text{Na}^+} \neq C_{\text{Cl}^-}$. It increases as the ionic strength of the pore solution decreases. The maximal ionic strength used in this study is 0.01 mol/L and the corresponding minimal thickness of the EDL is about 14 nm (Zhang & Wang, 2017). The grid size of the LBM in this study is 1 nm, which is sufficient to resolve the structure of the EDL. When the diffusion achieves steady state by solving the

Table 3
Overview of Parameters of the 3D Steady Diffusion Simulation of Ions in the Compacted Clay

Geometry and mesh	0.288				
Porosity	0.64; 0.68; 0.73; 1.0				
Water saturation S_w	0.64; 0.68; 0.73; 1.0				
Parameters in the transport model					
$D_{l,0}$ (m^2/s)	2.0×10^{-9}				
Concentration boundary of the transition region at the inlet C_{in} (mol/L)	1.0×10^{-7}				
Concentration boundary of the transition region at the outlet C_{out} (mol/L)	1.0×10^{-8}				
$\epsilon_r \epsilon_0$ ($C^2/J \cdot m$)	6.95×10^{-10}				
Simulation cases					
No.	1	2	3	4	5
Diffusion coefficient in the liquid phase $D(r)$	$D_{l,0}$	Equation 20	Equation 20	$D_{l,0}$	$D_{l,0}$
Thickness of water film (nm)	0	0	1	0	0
Bulk electrolyte concentration $C_{l,0}$ (mmol/L)	10.0	10.0	10.0	10.0	5.0
Surface charge density σ_0 (C/m^2) of solid	-0.001	-0.001	-0.001	-0.01	-0.01

Poisson-Boltzmann-Nernst-Planck equations (cf. Equations 6 and 9), the effective diffusion coefficients can be calculated by Equation 11.

Regarding the diffusion coefficient and the presence of water films, similar scenarios as for the HTO simulations (cf. Section 3.1.2) are considered in this section: (a) constant diffusion coefficient $D_{l,0}$ without thin water films on the clay surface (cf. cases 1,4,5), (b) a variable diffusion coefficient in the liquid phase without thin water films (case 2), and (c) with thin water films (case 3). Figure 8 shows the dependence of D_e^* on water saturation. As the water saturation decreases, D_e^* for both, the sodium and iodide tracers exhibit a decrease, which is more pronounced than that of the HTO tracer (cf. red line in Figure 8). In fully saturated compacted clays, the effective diffusion coefficient of sodium ions has been observed to exceed the one of HTO (Bestel et al., 2018; Glaus et al., 2010). However, our simulation results show that HTO can have a higher effective diffusion coefficient than sodium ions under unsaturated conditions (water saturation less than 0.75) because HTO can also diffuse in the gas phase. This finding is consistent with experimental observations in partially saturated Callovo-Oxfordian claystones conducted by Savoye et al. (2012). At full water saturation, the employment of a changed diffusion coefficient relating to the distance to the solid surface (case 2) leads to a decrease in the calculated D_e^* of around 14% for sodium and 13% for iodide compared to that simulated using a constant diffusion coefficient (case 1). However, with decreasing saturation these differences slightly decrease to 11% for sodium tracer but increase to 22% for iodide tracer. This suggests that the diffusion of sodium near the surface contributes the major component of the total flux, and thus the desaturation has limited influence on the calculated D_e^* with and without considering a changed local diffusion coefficient. In contrast, desaturation can alter the diffusion pathway of iodide tracers from the bulk region to the near-surface region, resulting in a larger difference of D_e^* with and without considering a changed local diffusion coefficient in the partially saturated compacted clays. Besides, the difference in D_e^* between sodium and iodide tracers increases by a factor of about two when the water saturation decreases from 1.0 to 0.64 (Figure 9). This reveals that desaturation can enhance the EDL effect on ion diffusion in compacted clays. This is because a decrease in saturation causes a reduction in the bulk volume for ions in clays, which will promote the interaction between charged surfaces and ions. Besides, the desaturation also causes an increase in the normalized volume charge density, ρ_e^* , while a larger ρ_e^* indicates a stronger EDL effect. It means that ρ_e^* as a scaling factor for the EDL effect can also be suitable in the partially saturated clays. Involving the thin nanoscale water film (case 3) also leads to an approximately 30% increase in the value of D_e^* for iodide tracers at a saturation level of around 0.7 in comparison to case 2. This increase is distinctly lower than the one indicated by previous 2D simulations in clayrocks by Gimmi and Churakov (2019), who found an increase of at least 90% in the D_e^* for involving the nanoscale water film, since in the 2D case the water film can create more connective pathways for diffusion than that in 3D porous media.

Figures 10a–10d show the 3D phase distribution in the nanostructure as well as the distribution of the electric potential and the tracer concentrations for simulation case 2 at a water saturation of 0.728. The pore-scale model takes into account the non-overlapping and overlapping EDL structures in the 3D pore geometry. The electric potential decreases near the negatively charged surface in Figure 10b, and the cations exhibit a higher concentration than the anions due to the negative electric potential within the pores (Figures 10c and 10d). Our pore-scale model is capable of considering 3D pore geometries and the structures of partially or fully overlapping EDL in nanopores. For instance, the EDL

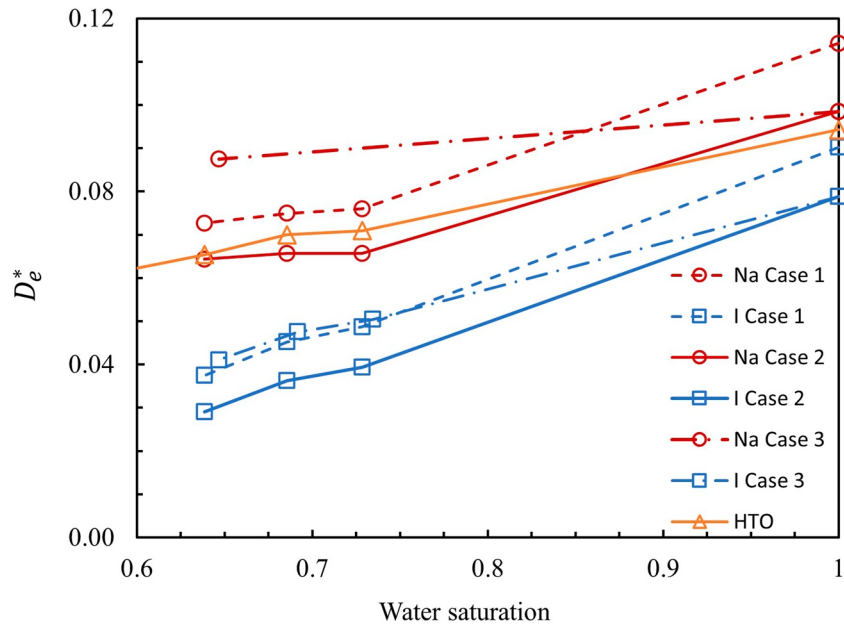


Figure 8. Simulated relative effective diffusion coefficients D_e^* of the $^{22}\text{Na}^+$ tracer (red lines) and the $^{125}\text{I}^-$ tracer (blue lines) in the compacted clay as a function of water saturation. The dashed lines use a constant diffusion coefficient (cf. case 1 in Table 3); the solid lines by location-dependent diffusion coefficient (case 2 in Table 3); and the dash-point line addresses the adding of a thin water film (case 3 in Table 3). The orange line represents the HTO tracer (cf. the orange solid line in Figure 7).

within Pore 1 (indicated by the black square in Figure 10a) is fully overlapping, while that in Pore 2 (indicated by the red square in Figure 10a) is only partially overlapping. Figures 11a–11d compare the distributions of the electric potential and the tracer concentrations along the radial direction (indicated by the arrows in Figure 9a). Our pore-scale simulations reveal an exponential decrease in the electrical potential near the surface of the clay particles. By comparing the electrical potential distributions in Pores 1 and 2, we find that the electric potential in the pore with completely overlapping EDL (Pore 1) has a more homogeneous distribution than that in the pore

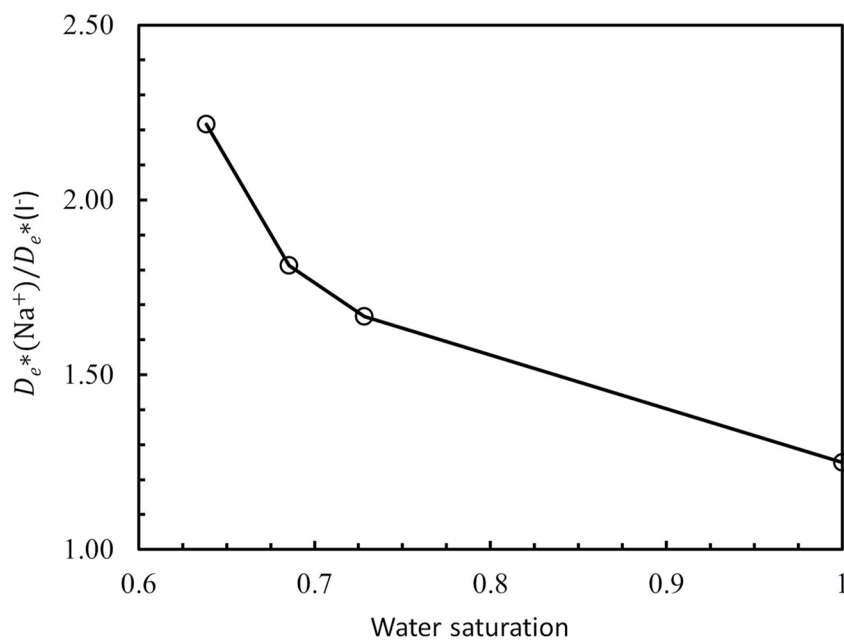


Figure 9. $D_e^*(\text{Na}^+)/D_e^*(\text{I}^-)$ as a function of water saturation for simulation case 2.

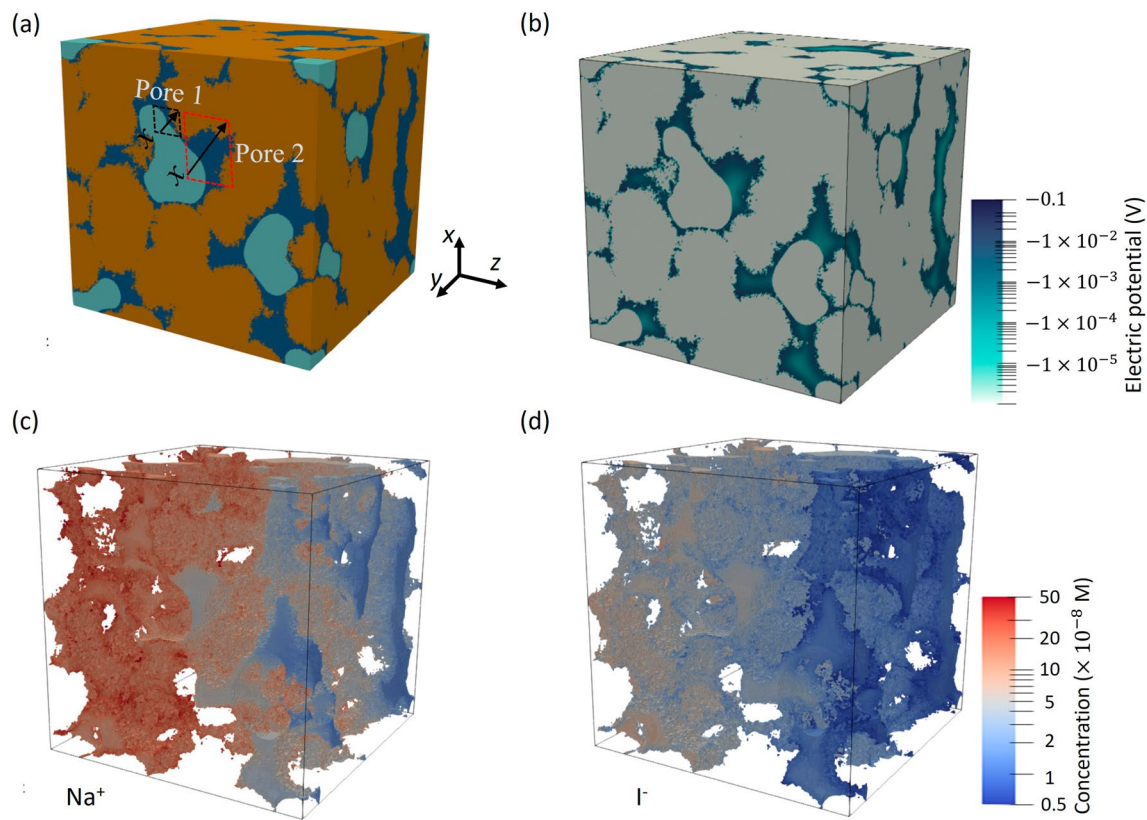


Figure 10. Simulated local distributions of phases (a), electric potential (b) and tracer concentrations (c, d) in the generated nanostructure for simulation case 2 (location-dependent diffusion coefficient) at a water saturation of 0.728. In Figure (a), the brown, dark blue and tight blue phases represent the clay particles, the liquid and the gas phase, respectively. The solid and gas phases are hyaline and invisible in (c, d).

with partially overlapping EDL (Pore 2). Furthermore, the mean-concentration ratio between sodium and iodide decreases from 4.1 in Pore 1 to 1.2 in Pore 2 when the thickness of the water films increases from 4 to 33 nm. This EDL effect is different from our previous study of fully saturated compacted clays (Wu et al., 2020), where the overlapping EDL could significantly enhance the EDL effect on ion diffusion. In unsaturated compacted clays, the non-charged gas-liquid interface weakens the EDL effect in the overlapping EDL. This suggests that the EDL in unsaturated compacted clays exhibits a more complex and nonlinear influence on ion diffusion than under fully saturated conditions.

3.3. Comparison With Reported Experimental Data

Figure 12 compares the simulation results with experimental data measured in compacted sedimentary rocks (García-Gutiérrez et al., 2023) and illite/sand mixtures (Savoie et al., 2014). The experimental data obtained for Callovo-Oxfordian (COx) claystones (Savoie et al., 2010, 2012) and compacted kaolinite (Wang et al., 2022) are also depicted for comparison. While unsaturated conditions in the compacted sedimentary rocks were obtained by the equilibrium method, in other cases the osmotic method was used to control the suction. Our simulated relative effective diffusion coefficients D_e^* for HTO and the anionic tracer iodide agree well with the experimental data from García-Gutiérrez et al. (2023). However, the experimental data obtained using the osmotic method shows a sharper drop than our simulation results. This discrepancy could be attributed to two primary reasons: (a) a non-equilibrium state of water and pressure distributions in samples using the osmotic methods; and (b) an inconsistency of the pore geometries between our regenerated clay and the real samples.

The osmotic method is used to control the suction and to reduce the pressure of the pore water below its saturation vapor pressure, thereby inducing the vaporization of pore water (Delage & Cui, 2008; Lloret Morancho et al., 2003). The time required to reach equilibrium in the osmotic method depends on the abilities of water/vapor migration and pressure evolution. In a tight porous material, the time to reach equilibrium may be significant. For

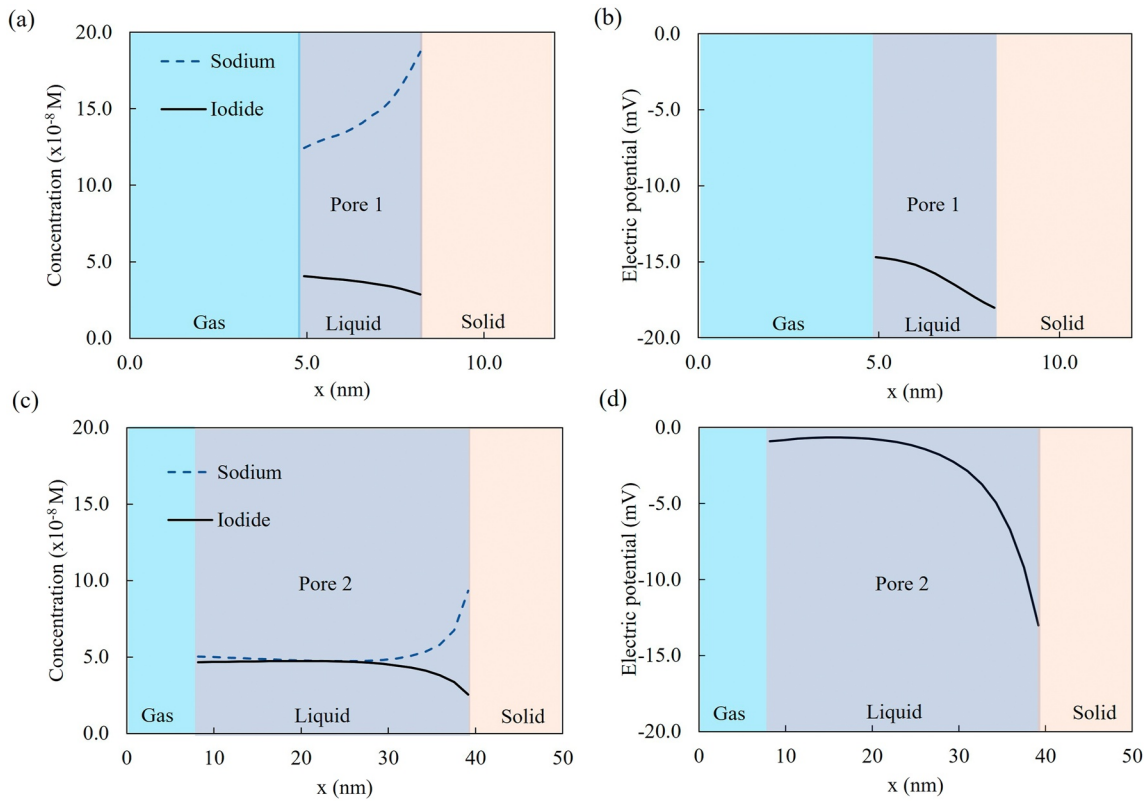


Figure 11. Distribution of tracers (a, c) and electric potential (b, d) in Pore 1 (a, b) and Pore 2 (c, d) along the radial directions (arrow x) shown in Figure 10 (a).

example, a previous study (Delage & Cui, 2008) demonstrated that a sample of compacted Jossigny silt under the suction of 800 kPa requires approximately 1 month to reach equilibrium, which is much longer than for sandy soils. Before reaching equilibrium, the pressure changes closer to the boundaries will first cause the pore water to vaporize. Hence, the water saturation profiles exhibit a rough U-shape, as observed in shale (Nunn et al., 2018), with a lower water saturation at the inlet and outlet boundaries and a higher saturation in the center. Additionally, the pressure gradient could also induce a deformation of the clay material (Guo & Fall 2021; Ma et al., 2020). This hydromechanical coupled effect on the evolution of pressure p in clay materials can be described by the Richards's model (Chen et al., 2022; Miller et al., 1998):

$$(C_w + S_e k_e) \frac{\partial p}{\partial t} + \nabla \cdot \left(-\frac{\kappa}{\mu} \nabla p \right) = 0, \quad (34)$$

where $C_w = -\partial\theta/\partial p$ is the specific moisture capacity, S_e the water saturation, k_e the effective compressibility, κ the permeability of the porous medium, and μ the dynamic viscosity of water. For a one-dimensional system under the condition of $S_e \approx 1$, the above equation can be simplified as:

$$\frac{\partial p}{\partial t} = \frac{\kappa}{\mu(C_w + k_e)} \frac{\partial^2 p}{\partial x^2}, \quad (35)$$

and k_e can be estimated from the compressibilities of rock k_s and water k_w by the formula: $k_e = \theta k_w + (1 - \theta)k_s$. Therefore, the characteristic time for pressure equilibration is $t^* = L^2 \mu (C_w + k_e) / \kappa$. Assuming that the porosity of the rock matrix has a very low susceptibility to pressure in comparison to water, $C_w = -\partial\theta/\partial p \approx 0$. Hence, t^* can be simplified as: $t^* = k_e L^2 \mu / \kappa$. The estimated values of the above parameters are $\theta = 0.3$, $k_w = 1 \times 10^{-7} 1/\text{Pa}$ (Domenico & Mifflin, 1965), $L = 1 \text{ cm}$, $\mu = 10^{-3} \text{ Pa}\cdot\text{s}$, and $\kappa = 10^{-20} \text{ m}^2$ (Rolfe & Aylmore, 1977) result in $t^* \approx 12$ days. This is the characteristic time for the condition of nearly full saturation. However, as the water saturation decreases, the permeability sharply decreases, and the effective compressibility increases. This can slowdown the expulsion of porewater from the interior, and therefore the characteristic time t^* will increase significantly. As a result, it

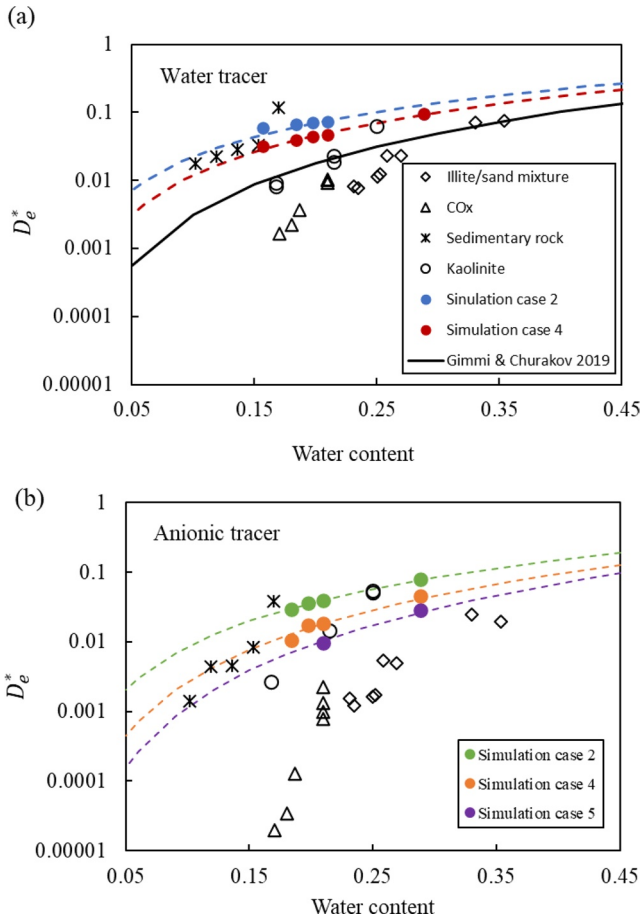


Figure 12. Comparisons of D_e^* given by the simulations of this work with reported experimental data and simulations for water tracers (i.e., deuterated and tritiated water) (a) and anionic tracers (b) as a function of water content φ_w . The experimental data are indicated by different black markers. The colored circles refer to the simulations performed in this work: blue and red are case 2 and case 4 in Table 2; green, orange and purple: case 2, case 4 and case 5 in Table 3, respectively. The black solid line refers to the fitting formula $D_e^*/D_0 = \varphi_w^{2.5}$ from previous 2D simulations (Gimmi & Churakov, 2019). Dashed lines are the best-fitting curves of the simulation results (red: $D_e^*/D_0 = \varphi_w^{1.92}$; blue: $D_e^*/D_0 = \varphi_w^{1.65}$; green: $D_e^*/D_0 = \varphi_w^{2.07}$; orange: $D_e^*/D_0 = \varphi_w^{2.57}$ and purple: $D_e^*/D_0 = \varphi_w^{2.93}$).

may take several months for a compacted clay sample with a thickness of only 1 cm to achieve an equilibrium state. Before reaching an equilibrium state, the water saturation profiles will display a U-shape. This heterogeneous distribution of saturation at the inlet and outlet boundaries could have a notable impact on the measured effective diffusion coefficients.

The transport properties of a material depend strongly on its pore geometry. Thus, for the purpose of performing more accurate pore-scale simulations, it is critical to employ more realistic 3D microstructures of clays. Recent improvements in 3D imaging techniques, such as Nano X-ray Computed Tomography (nanoCT) and Focused Ion Beam Scanning Electron Microscopes (FIB-SEM), have extended the view of researchers from submicroscale to nanoscale 3D porous geometries (Keller & Holzer, 2018). Additionally, the rapid evolution of artificial intelligence (AI) and machine learning (ML) also significantly improves the methodology to automatically generate a set of 3D microstructures using low-resolution 3D microstructures or 2D slices of a porous material (Huang et al., 2022; Zheng & Zhang, 2022). The nanostructure used in this study was generated by the QSGS method for granular materials, which can satisfy statistical properties of porosity, specific surface area, and mean particle/pore size, but cannot account for the different topological characteristics of the various clay materials. This limitation could be addressed in future studies by refining and testing different microstructural models as well as by exploiting the latest developments in the field like employing and extending the generative adversarial network (GAN) model (Gayon-Lombardo et al., 2020; Kench & Cooper, 2021) to generate more reliable 3D microstructures of clay materials.

3.4. Pore-Scale Implication and Prospects

The compressed EDL caused by the desaturation in clay minerals may induce a complex two-way coupling between the electrokinetic effect and the ion diffusion. This effect is particularly pronounced within the thin nanoscale water films, where molecular interactions at both liquid/gas and liquid/solid interfaces can magnify the desaturation impact on solute transport (Bjorneholm et al., 2016). However, it is a challenge to understand this coupled process in clays using the continuum-scale models fitted with experimental results. Molecular simulations, constrained by the massive computational cost, typically concentrate on solute transport within a single nanopore. The proposed pore-scale model is a versatile bridging tool, aiming to integrate molecular-scale data into continuum-scale models (upscaling), which would establish processes-based relationships. This study quantifies various effects (such as water films, pore-size dependent diffusion coefficients in the liquid phase, and/or EDL effects) on solute diffusion in partially saturated nanoporous media. The pore-scale view from this study has important implications for the quantification of solute transport in partially saturated clays, which is also helpful for future experimental design and evaluating radionuclide migration in the near and far field of deep geological repositories. The simulations conducted in this study were run within hours to reach the steady state, which is more time-efficient and cost-effective compared to experiments.

In addition, the proposed pore-scale model can also extend to include the complex electrokinetic properties of the gas/liquid interface (Levin et al., 2009; Olivieri et al., 2018), which could also have an influence on the transport of ions in the liquid phase of compacted clays (Kallay et al., 2014; Olivieri et al., 2018). For example, The zeta potential of gas bubbles in the aqueous electrolyte is reported to range from -30 mV to -45 mV at pH = 7, as measured by Yang et al. (2001) and Takahashi (2005). This could have a non-negligible impact on the ion transport in clay materials at a low water saturation. Besides, previous MD simulations (Churakov, 2013; Le Crom et al., 2021) indicated that the diffusion coefficients of cations confined in the thin water film drastically increase

on the surface of montmorillonites and the average water diffusion coefficient within the thin water film is also larger than that in the water-saturated system. Further experiments and MD simulations are still needed to improve the understanding of the gas/liquid interface effect on solute transport in clays and clayrocks. During the drying process in the smectite mineral, the previous study shows that the average interparticle distance decreases while the number of sheets per clay particle increases, which suggests a nanoscale structural modification and reorganization of clay materials during the hydration process (Seiphoori et al., 2014). These changes could alter the pathway for solute diffusion and impact the relationship of the effective diffusion coefficient with saturation. The development of hydromechanical coupled pore-scale models could shed light on these processes. For instance, Chen et al. (2018) employed a hydro-mechanical coupled LBM-DEM model to investigate the hydraulic fracture propagation in rocks with cemented natural fractures. Kim et al. (2021) developed a coupled multiphase fluid flow and discrete fracturing model to study gas migration in compacted bentonite. Pore-scale models that account for these hydromechanical coupling effects in clays during desaturation are expected to enhance the understanding of the mechanisms governing water and vapor transport under the mechanical deformation of clay particles.

4. Conclusions

A numerical framework was developed to simulate water and ion diffusion in 3D partially saturated pore geometries of clays. By assuming that the clay nanostructures are isotropic and rigid, this numerical framework first generates a pore geometry of a compacted clay at a nanoscale resolution by the QSGS method. The two-phase single-component Shan-Chen LBM model was then used to simulate the vapor-water distribution in complex 3D pore geometries with a homogeneous wettability at the pore scale (Section 2.1). This study considers several conditions for water and ion diffusion including constant or variable diffusion coefficients in the liquid phase and the consideration of thin water films on the solid surface as a solute transport pathway. An equivalent solute method (cf. Section 2.4) benchmarked against analytical solutions was also developed to improve the numerical stability affected by the significant discontinuities through the liquid/gas interface in concentration and diffusion coefficients of HTO at the steady state. Excluding the steric effect, Fick's law was numerically solved by LBM to simulate water diffusion in clays, while the coupled Poisson-Boltzmann-Nernst-Planck equations were solved to simulate ion diffusion under the influence of the EDL effect. Our investigations showed that as water saturation decreases, the relative effective diffusion coefficients for both cationic and anionic tracers decrease more pronounced than the one for HTO. The model was designed to quantify the impact of water films on HTO diffusion showing an increase in D_e^* in the clay at lower water saturation compared to the simulation case neglecting the water film, which is consistent with previous experimental investigations (Tokunaga et al., 2017).

In addition, our model reveals that desaturation can enhance the EDL effect on ion diffusion in compacted clays since a decrease in saturation causes an increase in ρ_e^* (normalized volume charge density), a dimensionless parameter quantifying the EDL effect on ion diffusion. Using pore-scale simulations, the local distributions of electrical potential and concentrations of tracers can be obtained in every single pore. By comparing these distributions, we found that the EDL in unsaturated compacted clays exhibits a more complex and nonlinear influence on ion diffusion than indicated by previous pore-scale simulations under saturated conditions (Yang & Wang, 2019). The predicted effective diffusion coefficients show good agreement with experimentally derived data for compacted sedimentary rocks. Some discrepancies were observed for clay and clayrock samples equilibrated with osmotic methods, which can be attributed to differences in pore geometry and the non-equilibrium distribution of water in the experiments. The developed modeling approach will be extended to include further process couplings, for example, with respect to hydromechanical effects or the electrokinetic properties of the gas/liquid interface, that will impact solute diffusion pathways and consequently the effective diffusion coefficients of solutes.

This study provides mechanistic insights into coupled transport of solutes in partially saturated clay-based materials and a solid basis for evaluating radionuclide migration in the near and far field of deep geological repositories. These insights at the pore scale can be implemented in larger scale analyses for example, in continuum-scale simulations for the evaluation of radionuclide migration in a repository system by considering the constitutive equations with upscaled parameters (cf. best-fitting formulas in Figure 12) in multi-phase and multicomponent reactive transport approaches (Ahmadi et al., 2022). Besides, the findings in partially saturated clay-based materials from this study are also relevant for a wide range of environmental and engineering processes such as contaminant transport in aquitards (Muniruzzaman & Rolle, 2019), bio-reactive transport of hydrogen storage (Zivar et al., 2021), and geological CO₂ sequestration (Li et al., 2017).

Data Availability Statement

The data used in this study are detailed in the paper. The relative effective diffusion coefficients and output data (e.g., Figures 6 and 10) given by our model are available online (<https://doi.org/10.26165/JUELICH-DATA/JINHGU>).

Acknowledgments

The project leading to this application has received funding from the European Union's Horizon 2020 research and innovation programme under grant agreement No 847593 (EURAD WP DONUT). Y. Y., G. D., and D. B. acknowledge funding by the German Federal Ministry of Education and Research (BMBF, Grant 02NUK053A) and the Innovation and Networking Fund of the Helmholtz Association (Grant SO-093 - iCross). J. P. acknowledges funding from the European Research Council through the project GENIES (ERC, grant agreement 101040341). Y. Y. gratefully acknowledges the computing time granted by the JARA Vergabegremium and provided on the JARA Partition part of the supercomputer JURECA at Forschungszentrum Jülich.

References

- Ahmadi, N., Muniruzzaman, M., Sprocati, R., Heck, K., Mosthaf, K., & Rolle, M. (2022). Coupling soil/atmosphere interactions and geochemical processes: A multiphase and multicomponent reactive transport approach. *Advances in Water Resources*, *169*, 104303. <https://doi.org/10.1016/j.advwatres.2022.104303>
- Appelo, C. A. J., Van Loon, L. R., & Wersin, P. (2010). Multicomponent diffusion of a suite of tracers (HTO, Cl, Br, I, Na, Sr, Cs) in a single sample of Opalinus Clay. *Geochimica et Cosmochimica Acta*, *74*(4), 1201–1219. <https://doi.org/10.1016/j.gca.2009.11.013>
- Bag, R., & Jadda, K. (2021). Influence of water content and dry density on pore size distribution and swelling pressure of two Indian bentonites. *Bulletin of Engineering Geology and the Environment*, *80*(11), 8597–8614. <https://doi.org/10.1007/s10064-021-02459-0>
- Bentz, J., Patel, R. A., Benard, P., Lieu, A., Hauptenthal, A., & Kroener, E. (2022). How heterogeneous pore scale distributions of wettability affect infiltration into porous media. *Water*, *14*(7), 1110. <https://doi.org/10.3390/w14071110>
- Bestel, M., Glaus, M. A., Frick, S., Gimmi, T., Juranyi, F., Van Loon, L. R., & Diamond, L. W. (2018). Combined tracer through-diffusion of HTO and ²²Na through Na-montmorillonite with different bulk dry densities. *Applied Geochemistry*, *93*, 158–166. <https://doi.org/10.1016/j.apgeochem.2018.04.008>
- Birgersson, M. (2017). A general framework for ion equilibrium calculations in compacted bentonite. *Geochimica et Cosmochimica Acta*, *200*, 186–200. <https://doi.org/10.1016/j.gca.2016.11.010>
- Bjornholm, O., Hansen, M. H., Hodgson, A., Liu, L. M., Limmer, D. T., Michaelides, A., et al. (2016). Water at interfaces. *Chemical Reviews*, *116*(13), 7698–7726. <https://doi.org/10.1021/acs.chemrev.6b00045>
- Bourg, I. C., Sposito, G., & Bourg, A. C. M. (2007). Modeling cation diffusion in compacted water-saturated sodium bentonite at low ionic strength. *Environmental Science & Technology*, *41*(23), 8118–8122. <https://doi.org/10.1021/es0717212>
- Chen, Y.-F., Ye, Y., Hu, R., Yang, Z., & Zhou, C.-B. (2022). Modeling unsaturated flow in fractured rocks with scaling relationships between hydraulic parameters. *Journal of Rock Mechanics and Geotechnical Engineering*, *14*(6), 1697–1709. <https://doi.org/10.1016/j.jrmge.2022.02.008>
- Chen, Z., Yang, Z., & Wang, M. (2018). Hydro-mechanical coupled mechanisms of hydraulic fracture propagation in rocks with cemented natural fractures. *Journal of Petroleum Science and Engineering*, *163*, 421–434. <https://doi.org/10.1016/j.petrol.2017.12.092>
- Churakov, S. V. (2013). Mobility of Na and Cs on montmorillonite surface under partially saturated conditions. *Environmental Science & Technology*, *47*(17), 9816–9823. <https://doi.org/10.1021/es401530n>
- Delage, P., & Cui, Y. J. (2008). An evaluation of the osmotic method of controlling suction. *Geomechanics and Geoengineering*, *3*(1), 1–11. <https://doi.org/10.1080/17486020701868379>
- Domenico, P. A., & Mifflin, M. D. (1965). Water from low-permeability sediments and land subsidence. *Water Resources Research*, *1*(4), 563–576. <https://doi.org/10.1029/WR001i004p00563>
- Duncan, J. S. (1992). In *Introduction to colloid and surface chemistry*. Elsevier Science Ltd.
- García-Gutiérrez, M., Mingarro, M., Morejón, J., Alonso, U., & Missana, T. (2023). Analysis of the role of water saturation degree in HTO, ³⁶Cl, and ⁷⁵Se diffusion in sedimentary rock. *Minerals*, *13*(5), 593. <https://doi.org/10.3390/min13050593>
- Gayon-Lombardo, A., Mosser, L., Brandon, N. P., & Cooper, S. J. (2020). Pores for thought: Generative adversarial networks for stochastic reconstruction of 3D multi-phase electrode microstructures with periodic boundaries. *Npj Computational Materials*, *6*(1), 82. <https://doi.org/10.1038/s41524-020-0340-7>
- Gimmi, T., & Alt-Epping, P. (2018). Simulating Donnan equilibria based on the Nernst-Planck equation. *Geochimica et Cosmochimica Acta*, *232*, 1–13. <https://doi.org/10.1016/j.gca.2018.04.003>
- Gimmi, T., & Churakov, S. V. (2019). Water retention and diffusion in unsaturated clays: Connecting atomistic and pore scale simulations. *Applied Clay Science*, *175*, 169–183. <https://doi.org/10.1016/j.clay.2019.03.035>
- Glaus, M. A., Frick, S., Rossé, R., & Loon, L. R. V. (2010). Comparative study of tracer diffusion of HTO, ²²Na⁺ and ³⁶Cl⁻ in compacted kaolinite, illite and montmorillonite. *Geochimica et Cosmochimica Acta*, *74*(7), 1999–2010. <https://doi.org/10.1016/j.gca.2010.01.010>
- Glaus, M. A., Frick, S., & Van Loon, L. R. (2020). A coherent approach for cation surface diffusion in clay minerals and cation sorption models: Diffusion of Cs⁺ and Eu³⁺ in compacted illite as case examples. *Geochimica et Cosmochimica Acta*, *274*, 79–96. <https://doi.org/10.1016/j.gca.2020.01.054>
- Guo, G., & Fall, M. (2021). Advances in modelling of hydro-mechanical processes in gas migration within saturated bentonite: A state-of-art review. *Engineering Geology*, *287*, 106123. <https://doi.org/10.1016/j.enggeo.2021.106123>
- Guo, Y., He, X., Huang, W., & Wang, M. (2018). Microstructure effects on effective gas diffusion coefficient of nanoporous materials. *Transport in Porous Media*, *126*(2), 431–453. <https://doi.org/10.1007/s11242-018-1165-4>
- Gvirtzman, H., & Gorelick, S. M. (1991). Dispersion and advection in unsaturated porous media enhanced by anion exclusion. *Nature*, *352*(6338), 793–795. <https://doi.org/10.1038/352793a0>
- Hsiao, Y.-W., & Hedström, M. (2015). Molecular dynamics simulations of NaCl permeation in bihydrated montmorillonite interlayer nanopores. *Journal of Physical Chemistry C*, *119*(30), 17352–17361. <https://doi.org/10.1021/acs.jpcc.5b01169>
- Huang, H., Sukop, M., & Lu, X. (2015). *Multiphase Lattice Boltzmann methods: Theory and application*. John Wiley & Sons.
- Huang, Y., Xiang, Z., & Qian, M. (2022). Deep-learning-based porous media microstructure quantitative characterization and reconstruction method. *Physical Review*, *105*(1–2), 015308. <https://doi.org/10.1103/PhysRevE.105.015308>
- Jungwirth, P., & Tobias, D. J. (2002). Ions at the air/water interface. *The Journal of Physical Chemistry B*, *106*(25), 6361–6373. <https://doi.org/10.1021/jp020242g>
- Kallay, N., Preocanin, T., Selmani, A., Kovačević, D., Lützenkirchen, J., Nakahara, H., & Shibata, O. (2014). Thermodynamic model of charging the gas/water interface. *Journal of Physical Chemistry C*, *119*(2), 997–1007. <https://doi.org/10.1021/jp507477u>
- Keller, L. M., & Holzer, L. (2018). Image-based upscaling of permeability in Opalinus Clay. *Journal of Geophysical Research: Solid Earth*, *123*(1), 285–295. <https://doi.org/10.1002/2017jb014717>
- Kench, S., & Cooper, S. J. (2021). Generating three-dimensional structures from a two-dimensional slice with generative adversarial network-based dimensionality expansion. *Nature Machine Intelligence*, *3*(4), 299–305. <https://doi.org/10.1038/s42256-021-00322-1>

- Kim, K., Rutqvist, J., Harrington, J. F., Tamayo-Mas, E., & Birkholzer, J. T. (2021). Discrete dilatant pathway modeling of gas migration through compacted bentonite clay. *International Journal of Rock Mechanics and Mining Sciences*, *137*, 104569. <https://doi.org/10.1016/j.ijrmps.2020.104569>
- Krishna, R., & van Baten, J. M. (2012). Investigating the validity of the Bosanquet formula for estimation of diffusivities in mesopores. *Chemical Engineering Science*, *69*(1), 684–688. <https://doi.org/10.1016/j.ces.2011.11.026>
- Leão, T. P., & Tuller, M. (2014). Relating soil specific surface area, water film thickness, and water vapor adsorption. *Water Resources Research*, *50*(10), 7873–7885. <https://doi.org/10.1002/2013wr014941>
- Le Crom, S., Tournassat, C., Robinet, J.-C., & Marry, V. (2021). Influence of water saturation level on electrical double layer properties in a clay mineral mesopore: A molecular dynamics study. *Journal of Physical Chemistry C*, *126*(1), 647–654. <https://doi.org/10.1021/acs.jpcc.1c08637>
- Lee, J., Laoui, T., & Karnik, R. (2014). Nanofluidic transport governed by the liquid/vapour interface. *Nature Nanotechnology*, *9*(4), 317–323. <https://doi.org/10.1038/nnano.2014.28>
- Leroy, P., Jougnot, D., Revil, A., Lassin, A., & Azaroual, M. (2012). A double layer model of the gas bubble/water interface. *Journal of Colloid and Interface Science*, *388*(1), 243–256. <https://doi.org/10.1016/j.jcis.2012.07.029>
- Levin, Y., dos Santos, A. P., & Diehl, A. (2009). Ions at the air-water interface: An end to a hundred-year-old mystery? *Physical Review Letters*, *103*(25), 257802. <https://doi.org/10.1103/PhysRevLett.103.257802>
- Li, Q., Steefel, C. I., & Jun, Y. S. (2017). Incorporating nanoscale effects into a continuum-scale reactive transport model for CO₂-deteriorated cement. *Environmental Science & Technology*, *51*(18), 10861–10871. <https://doi.org/10.1021/acs.est.7b00594>
- Lloret Moranco, A., Villar, M. V., Sanchez, M., Gens Solé, A., Pintado Llubra, X., & Alonso Pérez de Agreda, E. (2003). Mechanical behaviour of heavily compacted bentonite under high suction changes. *Géotechnique*, *53*(1), 27–40. <https://doi.org/10.1680/geot.2003.53.1.27>
- Lu, J. H., Lei, H. Y., & Dai, C. S. (2019). Lattice Boltzmann equation for mass transfer in multi solvent systems. *International Journal of Heat and Mass Transfer*, *132*, 519–528. <https://doi.org/10.1016/j.ijheatmasstransfer.2018.12.010>
- Ma, T., Wei, C., Yao, C., & Yi, P. (2020). Microstructural evolution of expansive clay during drying–wetting cycle. *Acta Geotechnica*, *15*(8), 2355–2366. <https://doi.org/10.1007/s11440-020-00938-4>
- Miles, R. E., Reid, J. P., & Riipinen, I. (2012). Comparison of approaches for measuring the mass accommodation coefficient for the condensation of water and sensitivities to uncertainties in thermophysical properties. *Journal of Physical Chemistry A*, *116*(44), 10810–10825. <https://doi.org/10.1021/jp3083858>
- Miller, A. W., & Wang, Y. (2012). Radionuclide interaction with clays in dilute and heavily compacted systems: A critical review. *Environmental Science & Technology*, *46*(4), 1981–1994. <https://doi.org/10.1021/es203025q>
- Miller, C. T., Williams, G. A., Kelley, C. T., & Tocci, M. D. (1998). Robust solution of Richards' equation for nonuniform porous media. *Water Resources Research*, *34*(10), 2599–2610. <https://doi.org/10.1029/98wr01673>
- Mullet, M., Fievet, P., Reggiani, J. C., & Pagetti, J. (1997). Surface electrochemical properties of mixed oxide ceramic membranes: Zeta-potential and surface charge density. *Journal of Membrane Science*, *123*(2), 255–265. [https://doi.org/10.1016/S0376-7388\(96\)00220-7](https://doi.org/10.1016/S0376-7388(96)00220-7)
- Muniruzzaman, M., & Rolle, M. (2019). Multicomponent ionic transport modeling in physically and electrostatically heterogeneous porous media with PhreeqcRM coupling for geochemical reactions. *Water Resources Research*, *55*(12), 11121–11143. <https://doi.org/10.1029/2019wr026373>
- Nishiyama, N., & Yokoyama, T. (2021). Water film thickness in unsaturated porous media: Effect of pore size, pore solution chemistry, and mineral type. *Water Resources Research*, *57*(6), e2020WR029257. <https://doi.org/10.1029/2020wr029257>
- Nunn, J. A., Xiang, Y., & Al, T. A. (2018). Investigation of partial water saturation effects on diffusion in shale. *Applied Geochemistry*, *97*, 93–101. <https://doi.org/10.1016/j.apgeochem.2018.08.004>
- Olivieri, G., Parry, K. M., D'Auria, R., Tobias, D. J., & Brown, M. A. (2018). Specific anion effects on Na(+) adsorption at the aqueous solution-air interface: MD simulations, SESSA calculations, and photoelectron spectroscopy experiments. *Journal of Physical Chemistry B*, *122*(2), 910–918. <https://doi.org/10.1021/acs.jpcc.7b06981>
- Patel, R. A. (2018). Yantra: A Lattice Boltzmann method based tool for multiscale/multiphysics simulations. Retrieved from <http://bitbucket.org/yantralbm/yantra>
- Perko, J., & Patel, R. A. (2014). Single-relaxation-time Lattice Boltzmann scheme for advection-diffusion problems with large diffusion-coefficient heterogeneities and high-advection transport. *Physical Review*, *89*(5), 053309. <https://doi.org/10.1103/PhysRevE.89.053309>
- Probstein, R. F. (2005). *Physicochemical hydrodynamics: An introduction*. John Wiley & Sons.
- Revil, A., & Jougnot, D. (2008). Diffusion of ions in unsaturated porous materials. *Journal of Colloid and Interface Science*, *319*(1), 226–235. <https://doi.org/10.1016/j.jcis.2007.10.041>
- Revil, A., Linde, N., Cerepi, A., Jougnot, D., Matthäi, S., & Finsterle, S. (2007). Electrokinetic coupling in unsaturated porous media. *Journal of Colloid and Interface Science*, *313*(1), 315–327. <https://doi.org/10.1016/j.jcis.2007.03.037>
- Revil, A., Woodruff, W. F., & Lu, N. (2011). Constitutive equations for coupled flows in clay materials. *Water Resources Research*, *47*(5). <https://doi.org/10.1029/2010wr010002>
- Rolfé, P. F., & Aylmore, L. A. G. (1977). Water and salt flow through compacted clays: I. Permeability of compacted illite and montmorillonite. *Soil Science Society of America Journal*, *41*(3), 489–495. <https://doi.org/10.2136/sssaj1977.03615995004100030011x>
- Sander, R. (2015). Compilation of Henry's law constants (version 4.0) for water as solvent. *Atmospheric Chemistry and Physics*, *15*(8), 4399–4981. <https://doi.org/10.5194/acp-15-4399-2015>
- Savoye, S., Beaucaire, C., Fayette, A., Herbette, M., & Coelho, D. (2012). Mobility of cesium through the Callovo-Oxfordian claystones under partially saturated conditions. *Environmental Science & Technology*, *46*(5), 2633–2641. <https://doi.org/10.1021/es2037433>
- Savoye, S., Imbert, C., Fayette, A., & Coelho, D. (2014). Experimental study on diffusion of tritiated water and anions under variable water-saturation and clay mineral content: Comparison with the Callovo-Oxfordian claystones. *Geological Society, London, Special Publications*, *400*(1), 579–588. <https://doi.org/10.1144/sp400.9>
- Savoye, S., Page, J., Puente, C., Imbert, C., & Coelho, D. (2010). New experimental approach for studying diffusion through an intact and unsaturated medium: A case study with Callovo-Oxfordian argillite. *Environmental Science & Technology*, *44*(10), 3698–3704. <https://doi.org/10.1021/es903738t>
- Seiphoori, A., Ferrari, A., & Laloui, L. (2014). Water retention behaviour and microstructural evolution of MX-80 bentonite during wetting and drying cycles. *Géotechnique*, *64*(9), 721–734. <https://doi.org/10.1680/geot.14.P.017>
- Shan, X., & Chen, H. (1993). Lattice Boltzmann model for simulating flows with multiple phases and components. *Physical Review*, *47*(3), 1815–1819. <https://doi.org/10.1103/physreve.47.1815>
- Shan, X., & Chen, H. (1994). Simulation of nonideal gases and liquid-gas phase transitions by the Lattice Boltzmann equation. *Physical Review*, *49*(4), 2941–2948. <https://doi.org/10.1103/physreve.49.2941>
- Soler, J. M., Steefel, C. I., Gimmi, T., Leupin, O. X., & Cloet, V. (2019). Modeling the ionic strength effect on diffusion in clay: the DR-A experiment at Mont Terri. *ACS Earth and Space Chemistry*, *3*(3), 442–451. <https://doi.org/10.1021/acsearthspaccechem.8b00192>

- Sondi, I., Bišćan, J., & Praviđić, V. (1996). Electrokinetics of pure clay minerals revisited. *Journal of Colloid and Interface Science*, 178(2), 514–522. <https://doi.org/10.1006/jcis.1996.0146>
- Tachi, Y., & Yotsuji, K. (2014). Diffusion and sorption of Cs⁺, Na⁺, I⁻ and HTO in compacted sodium montmorillonite as a function of porewater salinity: Integrated sorption and diffusion model. *Geochimica et Cosmochimica Acta*, 132, 75–93. <https://doi.org/10.1016/j.gca.2014.02.004>
- Takahashi, M. (2005). ζ potential of microbubbles in aqueous solutions: Electrical properties of the gas–water Interface. *The Journal of Physical Chemistry B*, 109(46), 21858–21864. <https://doi.org/10.1021/jp0445270>
- Tamayo-Mas, E., Harrington, J. F., Brüning, T., Shao, H., Dagher, E. E., Lee, J., et al. (2021). Modelling advective gas flow in compact bentonite: Lessons learnt from different numerical approaches. *International Journal of Rock Mechanics and Mining Sciences*, 139, 104580. <https://doi.org/10.1016/j.ijrmmms.2020.104580>
- Tertre, E., Savoye, S., Hubert, F., Prêt, D., Dabat, T., & Ferrage, E. (2018). Diffusion of water through the dual-porosity swelling clay mineral vermiculite. *Environmental Science & Technology*, 52(4), 1899–1907. <https://doi.org/10.1021/acs.est.7b05343>
- Tian, H., Zhang, L., & Wang, M. (2015). Applicability of Donnan equilibrium theory at nanochannel-reservoir interfaces. *Journal of Colloid and Interface Science*, 452, 78–88. <https://doi.org/10.1016/j.jcis.2015.03.064>
- Tinnacher, R. M., Holmboe, M., Tournassat, C., Bourg, I. C., & Davis, J. A. (2016). Ion adsorption and diffusion in smectite: Molecular, pore, and continuum scale views. *Geochimica et Cosmochimica Acta*, 177, 130–149. <https://doi.org/10.1016/j.gca.2015.12.010>
- Tokunaga, T. K., Finsterle, S., Kim, Y., Wan, J., Lanzirotti, A., & Newville, M. (2017). Ion diffusion within water films in unsaturated porous media. *Environmental Science & Technology*, 51(8), 4338–4346. <https://doi.org/10.1021/acs.est.6b05891>
- Tournassat, C., Chapron, Y., Leroy, P., Bizi, M., & Boulahya, F. (2009). Comparison of molecular dynamics simulations with triple layer and modified Gouy–Chapman models in a 0.1M NaCl–montmorillonite system. *Journal of Colloid and Interface Science*, 339(2), 533–541. <https://doi.org/10.1016/j.jcis.2009.06.051>
- Underwood, T. R., & Bourg, I. C. (2020). Large-Scale molecular dynamics simulation of the dehydration of a suspension of smectite clay nanoparticles. *Journal of Physical Chemistry C*, 124(6), 3702–3714. <https://doi.org/10.1021/acs.jpcc.9b11197>
- Van Schaik, J., Kemper, W., & Olsen, S. (1966). Contribution of adsorbed cations to diffusion in clay-water systems. *Soil Science Society of America Journal*, 30(1), 17–22. <https://doi.org/10.2136/sssaj1966.03615995003000010013x>
- Vieceli, J., Roeselová, M., & Tobias, D. J. (2004). Accommodation coefficients for water vapor at the air/water interface. *Chemical Physics Letters*, 393(1–3), 249–255. <https://doi.org/10.1016/j.cplett.2004.06.038>
- Wang, J., Savoye, S., Ferrage, E., Hubert, F., Lefevre, S., Radwan, J., et al. (2022). Water and ion diffusion in partially-water saturated compacted kaolinite: Role played by vapor-phase diffusion in water mobility. *Journal of Contaminant Hydrology*, 248, 103989. <https://doi.org/10.1016/j.jconhyd.2022.103989>
- Wang, M., Wang, J., Pan, N., & Chen, S. (2007). Mesoscopic predictions of the effective thermal conductivity for microscale random porous media. *Physical Review*, 75(3), 036702. <https://doi.org/10.1103/PhysRevE.75.036702>
- Wigger, C., & Van Loon, L. R. (2018). Effect of the pore water composition on the diffusive anion transport in argillaceous, low permeability sedimentary rocks. *Journal of Contaminant Hydrology*, 213, 40–48. <https://doi.org/10.1016/j.jconhyd.2018.05.001>
- Wu, T., Yang, Y., Wang, Z., Shen, Q., Tong, Y., & Wang, M. (2020). Anion diffusion in compacted clays by pore-scale simulation and experiments. *Water Resources Research*, 56(11), e2019WR027037. <https://doi.org/10.1029/2019wr027037>
- Xu, R., Prodanović, M., & Landry, C. (2020). Pore-scale study of water adsorption and subsequent methane transport in clay in the presence of wettability heterogeneity. *Water Resources Research*, 56(10). <https://doi.org/10.1029/2020wr027568>
- Yang, C., Dabros, T., Li, D., Czarnecki, J., & Masliyah, J. H. (2001). Measurement of the Zeta potential of gas bubbles in aqueous solutions by microelectrophoresis method. *Journal of Colloid and Interface Science*, 243(1), 128–135. <https://doi.org/10.1006/jcis.2001.7842>
- Yang, Y., & Wang, M. (2018a). Pore-scale modeling of chloride ion diffusion in cement microstructures. *Cement and Concrete Composites*, 85, 92–104. <https://doi.org/10.1016/j.cemconcomp.2017.09.014>
- Yang, Y., & Wang, M. (2018b). Pore-scale study of thermal effects on ion diffusion in clay with inhomogeneous surface charge. *Journal of Colloid and Interface Science*, 514, 443–451. <https://doi.org/10.1016/j.jcis.2017.12.047>
- Yang, Y., & Wang, M. (2019). Cation diffusion in compacted clay: A pore-scale view. *Environmental Science & Technology*, 53(4), 1976–1984. <https://doi.org/10.1021/acs.est.8b05755>
- Yuan, T., Yang, Y., Ait-Mouheb, N., Deissmann, G., Fischer, C., Stumpf, T., & Bosbach, D. (2022). A comparative study on heterogeneity of clay rocks using pore-scale diffusion simulations and experiments. *Journal of Geophysical Research: Solid Earth*, 127(12), e2022JB025428. <https://doi.org/10.1029/2022jb025428>
- Zhang, L., & Wang, M. (2015). Modeling of electrokinetic reactive transport in micropore using a coupled Lattice Boltzmann method. *Journal of Geophysical Research: Solid Earth*, 120(5), 2877–2890. <https://doi.org/10.1002/2014jb011812>
- Zhang, L., & Wang, M. (2017). Electro-osmosis in inhomogeneously charged microporous media by pore-scale modeling. *Journal of Colloid and Interface Science*, 486, 219–231. <https://doi.org/10.1016/j.jcis.2016.09.057>
- Zheng, L., Rutqvist, J., Birkholzer, J. T., & Liu, H.-H. (2015). On the impact of temperatures up to 200°C in clay repositories with bentonite engineer barrier systems: A study with coupled thermal, hydrological, chemical, and mechanical modeling. *Engineering Geology*, 197, 278–295. <https://doi.org/10.1016/j.enggeo.2015.08.026>
- Zheng, Q., & Zhang, D. (2022). Digital rock reconstruction with user-defined properties using conditional generative adversarial networks. *Transport in Porous Media*, 144(1), 255–281. <https://doi.org/10.1007/s11242-021-01728-6>
- Zivar, D., Kumar, S., & Foroozesh, J. (2021). Underground hydrogen storage: A comprehensive review. *International Journal of Hydrogen Energy*, 46(45), 23436–23462. <https://doi.org/10.1016/j.ijhydene.2020.08.138>